J Nanopart Res (2022) 24:191
https://doi.org/10.1007/s11051-022-05573-6

RESEARCH PAPER

Green MoS_2 nanosheets as a promising material for decontamination of hexavalent chromium, pharmaceuticals, and microbial pathogen disinfection: spectroscopic study

Mohamed Eid M. Ali · Reem. Mohammed · Shimaa M. Abdel-Moniem · Mohamed Azab El-Liethy · Hanan S. Ibrahim

Received: 8 May 2022 / Accepted: 3 September 2022 / Published online: 16 September 2022
© The Author(s) 2022

Abstract Photoreduction of chromium hexavalent ions (Cr^{6+}) from the aquatic environment is urgently needed due to its impairing effect on human health. Adsorption, photoreduction, and desorption of reduced trivalent chromium (Cr^{3+}) at the photocatalyst surface are all significant factors for determining photocatalytic reduction efficiency. Herein, we report a facile, template-free hydrothermal approach to fabricate green and homogeneous mixed-phase (1 T/2H) molybdenum disulfide (MoS_2) nanosheets for highly efficient removal of Cr^{6+} ions and pharmaceuticals from wastewater. The nanostructure and morphology of the obtained (1 T/2H) MoS_2 are investigated; the calculated crystallite size of the (2H/1 T) MoS_2 nanosheets is found to be 1.7 nm. The presence of surface functional groups adsorption, and photoreduction processes is confirmed by spectroscopic studies using Fourier transform infrared (FTIR) spectra. Additionally, Raman spectra confirmed the formation of 1 T/2H mixed-phase MoS_2 which illustrates its crystal phases, structure, and chemical composition. Moreover, the point-of-zero charge analysis revealed the positively charged surface in the acid system. The obtained results revealed the non-toxicity of MoS_2 nanosheets at doses lower than 1000 ppm. The results reveal that the (1 T/2H) MoS_2 exhibited impressive reduction performance for Cr^{6+}; the reduction efficiency of chromium Cr^{6+} is 100% under simulated sunlight, 90 min at pH (3). Further spectroscopic study results confirm the importance of the adsorption step in Cr^{6+} ions photoreduction. Different pharmaceuticals are also completely degraded over (1 T/2H) MoS_2 nanosheets. Interestingly, complete removals of *E. coli* O157:H7, *Listeria monocytogenes*, and *Candida albicans* were observed at a dose of MoS_2 nanosheets of 250 ppm after a contact time of 30, 30, and 45 min, respectively. The results of the current work could lead to a rational design of high-performance nanosheets for the efficient decontamination of heavy metals, pharmaceuticals, and pathogens from aquatic environments.

Keywords Cr^{6+} ions · Cr^{3+} · (1 T/2H) MoS_2 · Antimicrobial · Photoreduction · Adsorption · Pharmaceuticals

I haven't submitted my manuscript to a preprint server prior to submission on journal of nanoparticle research.

Supplementary Information The online version contains supplementary material available at https://doi.org/10.1007/s11051-022-05573-6.

M. E. M. Ali · S. M. Abdel-Moniem · M. A. El-Liethy · H. S. Ibrahim
Water Pollution Research Department, Institute of Environmental Research and Climate Changes, National Research Centre, El-Buhouth St., Dokki, P.O. 12622, Cairo, Egypt

R. Mohammed (✉)
Physics Department, Faculty of Science, Aim Shams University, Abbassia, P.O. 11566, Cairo, Egypt
e-mail: reemmhmd11@sci.asu.edu.eg; reemmhmd11@yahoo.com

Introduction

Hexavalent chromium (Cr^{6+}) from industrial activities (such as electroplating, metal finishing, leather tanning, steel fabricating, photographic) are released into a water body, causing major environmental issues. Unfortunately, Cr^{6+} is known to be a mutagenic, carcinogenic, and toxic substance, which is harmful to biological systems and can easily enter the food chains [1]. Cr^{6+} concentrations in drinking water are regulated to 0.05 $mg.L^{-1}$ [2]. Subsequently, it is essential to eliminate Cr^{6+} from wastewater. Many researchers have been undergoing some efforts. There are traditional methods for reducing Cr^{6+} including bioremediation, ion exchange, membrane separation, adsorption, and chemical precipitation, but they all have problems such as sludge generation, damaged precipitation, and high operating costs [3–5]. For example, the adsorption technique is commonly utilized in the treatment of Cr^{6+} [6]. The challenge is that it can only be used for Cr^{6+} adsorption, and the desorbed Cr^{6+} still needs to be treated.

Transformation of Cr^{6+} to Cr^{3+} is one of the most popular ways of treating Cr^{6+} in wastewater [7]. Cr^{3+} is a necessary trace metal in human nutrition and is considered harmless [8–10]. Consequently, reducing Cr^{6+} to Cr^{3+} is considered a critical step in the treatment of wastewater containing Cr^{6+}. For the reduction of Cr^{6+}, many alternative procedures have been proposed, such as chemical reduction and photoreduction [11–13]. Among these techniques, photocatalysis utilizing sunlight is a promising method as it achieves the one-step elimination of Cr^{6+} [14, 15]. During the photocatalysis process, electron (e^-) and hole (h^+) active species are generated. These free radicals may recombine or contribute to redox processes. The photo-excited electrons at the catalyst surface can directly contribute to the reduction process, and can attack O_2 to produce active species $O_2^{\bullet-}$, H_2O_2, and $^{\bullet}OH$. Moreover, the photo-holes with a high oxidation potential can engage directly in the oxidation degradation process or oxidize water to form $^{\bullet}OH$. These active species $O_2^{\bullet-}$, H_2O_2, and $^{\bullet}OH$ can contribute to the complete breakdown of contaminants in CO_2 and water [15–17]. In the case of Cr^{6+}, electrons at the conduction band (CB) encourage the photoreduction process.

On the other hand, molybdenum disulfide (MoS_2) is an inorganic compound that contains one atom of molybdenum and two atoms of sulfur and belongs to the transition metal dichalcogenides (TMDs) series [18–20]. Due to its physical, chemical, and electronic properties, MoS_2 can be regarded as a promising semiconductor material that is widely used for photocatalytic processes, in addition to its great yield and cheap production. The direct bandgap of the MoS_2 monolayer is 1.8 eV. Moreover, its layered structure overcomes the graphene gapless problem [21], thus making it scientific and industrial importance. Preparing controllable MoS_2 nanosheets is one of the most challenging tasks, as MoS_2 has shown favorable and promising electron and quantum properties in the transition from bulk to two-dimensional (2D) structures [18, 22–25].

MoS_2 lattices have both 2H and 1 T phase models; 2H-MoS_2 (hexagonal phase) has semi-conducting behaviors, and its active sites exist only in the edges due to the localization of the d-band of transition metals [26, 27]. In addition, the 1 T phase (trigonal phase) has a metallic property. Fabrication of 1 T single-phase MoS_2 required highly toxic reaction sources and harsh reaction conditions. Consequently, it has been discovered that the hybrid phases 1T/2H MoS2 with the conductivity of the 1T phase and the handleability of the 2H phase can solve this problem and have a strong influence on its electronic properties, resulting in increased activity [26–28].

Of late, many procedures have been used to fabricate 1 T/2H MoS_2 nanostructures [29]. Among these procedures, the hydrothermal one enables the rapid production of a wide variety of structures. The photocatalytic activities of MoS_2 are investigated in reducing Cr^{6+} ions from an aqueous solution under simulating sunlight [30–32]. The generation of MoS_2 is generally based on the introduction of templates and surfactants, additional calcination processes, and indelible impurities, which can be disadvantageous at a high cost. Consequently, morphologically controllable production of 1 T/2H MoS_2 nanosheets using template-free methods remains a major challenge.

Herein, our current research aims to utilize the hydrothermal approach to prepare (2H/1 T) MoS_2 nanosheets without the use of surfactants, templates, or subsequent calcination processes that are used for photocatalytic reduction of Cr^{6+} ions and pharmaceuticals from aqueous solution. As well, the

antimicrobial activity of MoS_2 nanosheets is investigated. The photocatalytic efficiency of the photocatalytic reduction of Cr^{6+} to Cr^{3+} is examined in detail, including the effect of catalyst dose, solution pH, and the photocatalytic reduction mechanism. Moreover, the antimicrobial effects of MoS_2 nanosheets against microbial pathogens are studied.

Experimental work

Materials and reagent

Sodium molybdate anhydrate ($Na_6Mo_7O_{24}.4H_2O$) is supplied by Merck Chemicals Company, Germany. Thiourea (TU) (CH_4N_2S) and polyvinylpyrrolidone (PVP) ($(C_6H_9NO)_n$) powders ($\geq$99.0% in purity) are supplied by LOBA Chemie, India. Reagent grade potassium dichromate ($K_2Cr_2O_7$) is supplied by Sigma-Aldrich, USA. Cefadroxil, cefotaxime, meloxicam, ceftriaxone, paracetamol, and ciprofloxacin are purchased from Sigma-Aldrich, USA. All the chemicals employed are of analytical grade and applied without further purification. The solvent utilized in all the experimental procedures is deionized water.

Preparation method

Mixed-phase (2H/1 T) MoS_2 nanosheets are prepared using a simple hydrothermal route as illustrated in Fig. 1. Briefly, sodium molybdate anhydrate, thiourea, and polyvinylpyrrolidone are dissolved in 50 mL distilled water and stirred for 30 min. Then HCl is slowly added dropwise into the solution using a burette until the blue color is formed. The solution is stirred for a further 5 h, then transferred to an autoclave, and placed it in a muffle furnace at 180 °C for 24 h. The autoclave is allowed to come to room temperature and then filtrate the products, rinsing them with distilled water several times. The precipitate is then dried at 70 °C overnight. The dried MoS_2 powder is characterized and used for photocatalytic applications.

Characterization

Surface morphology and elemental analysis test of MoS_2 nanosheets are studied using a field emission scanning electron microscope (FE-SEM) and energy-dispersive X-ray spectroscopy (EDX) (QUANTA FEG250 at 20 kV). Equipped HR-TEM images are obtained using JEOL JEM-2100 high resolution of 0.19 nm at 200 kV (LaB6) to study the nanostructured MoS_2 nanosheets. The crystal phase of as-prepared products is characterized by X-ray diffraction (XRD, Bruker D8 Advance A25, Cu-Kα radiation, 40 kV, 40 mA). To investigate the composition and phase structure, the raman spectrum is collected on Pro-Raman, Enwave Optronics, at excitation wavelength lex 532 nm. Fourier transform infrared spectrum (JASCO FT/IR-4600 in the spectral range from 400 to 4000 cm^{-1}, with a resolution of 4 cm^{-1}) is used to study the surface structure of MoS_2 before and after adsorption and reduction. The pH value is measured with a pH meter (Orion versa star L1/5). The UV–vis spectra of the samples are measured on UV–vis spectrometer (JASCO-V-730). The concentration of total chromium are determined by inductively coupled plasma (ICP) emission spectroscopy (VISTA-MPX). The BET specific surface area (BET) measurement by N_2 adsorption/desorption is determined using a BET analyzer (ASAP-2020, Micromeritics). The pore volume and pore diameter distribution are derived from the adsorption isotherms by the Barrett-Joyner-Halenda (BJH) model. Zeta potential of the MoS_2 is measured by "Malvern Zetasizer Nano ZS."

Activity investigation

Adsorption process

First, a proper amount of K2Cr2O7 is dissolved in deionized water to prepare a 1000 ppm stock Cr^{6+} solution. Diluting this stock solution to produce a working solution with a known Cr^{6+} concentration. The initial solution pH is adjusted by using 0.1 N HCl and 0.1 N NaOH. A series of experiments are carried out by varying the contact time, the catalyst dose, and solution pH to examine the Cr^{6+} adsorption, and reduction performances of the prepared catalyst. All experiments are performed in duplicate and average results are reported. For typical adsorption runs, 0.2 g. L-1 of (2H/1T) MoS2 catalyst dispersion in a Cr^{6+} solution with an initial concentration of 20 ppm at pH 3 has been used. The mixture is stirred for 30 min under the dark condition to reach adsorption–desorption equilibrium. During the adsorption process, 3 mL of suspension is taken out by syringe filter (PTFE 0.45 µm) in regular 5-min intervals to obtain the supernatant.

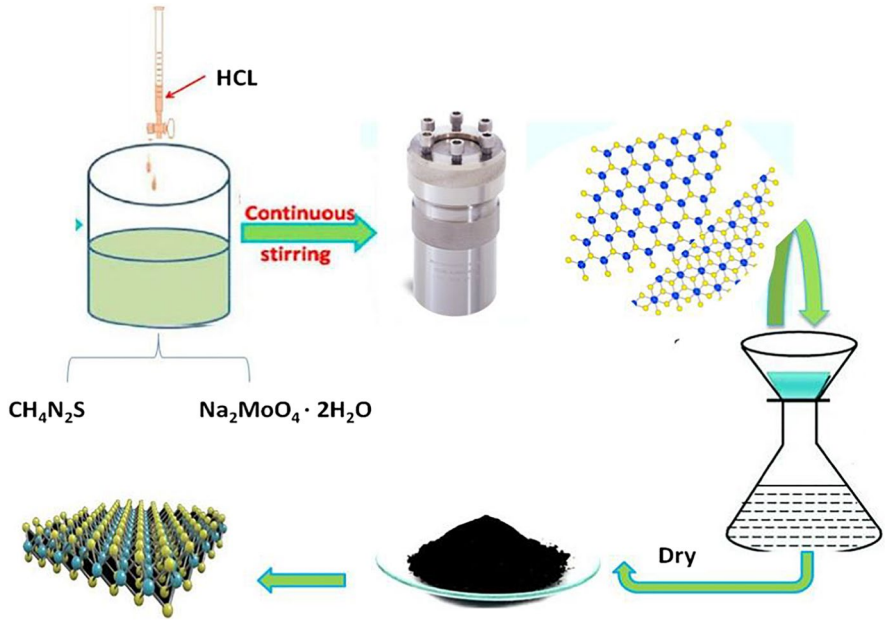

Fig. 1 Proposed diagram for mixed-phase (1 T/2H) MoS_2 nanosheet preparation

The Cr^{6+} concentration is determined by colorimetry at 540 nm using the diphenyl carbazide technique and by using a UV–vis spectrophotometer at 348 nm [33]. The amounts of total chromium are determined by inductively coupled plasma (ICP) [30]. The concentration of C^{3+} is calculated from Eq. (1) (the total chromium subtracting the Cr^{6+} concentration):

$$cr^{3+} = cr(total) - cr^{6+} \tag{1}$$

Adsorption percentage can be calculated as follows:

$$Adsorption\ \% = \frac{c_0 - c_t}{c_0} \times 100 \tag{2}$$

where C_o and C_t are the concentrations before and after different irradiation times.

Photoreduction process

After the adsorption process, the contact solution is exposed to the solar simulator. During the photoreduction process, 3 mL of suspension is taken out in a regular 30-min interval by syringe filter to obtain the supernatant. The concentration of Cr^{6+} in the supernatant is evaluated by using a UV–vis spectrophotometer and by the diphenyl carbazide method. The changes in Cr^{6+} concentration are determined by the formula.

Degradation % is calculated as follows:

$$Degradation\ \% = \frac{c_0 - c_t}{c_0} \times 100 \tag{3}$$

where C_o and C_t are the concentrations before and after different irradiation times, respectively. The isotherm and kinetic parameters are also calculated for photocatalytic reactions.

Determination of pH zero charge point

The point-of-zero charges (pH_{ZPC}) of the (2H/1 T) MoS_2 nanosheets are measured using the pH drift method [32]. In this method, the pH_{ZPC} of the (2H/1 T) MoS_2 photocatalyst is determined by adding 25 mL of 0.1 N NaCl in 50-mL conical high-density polystyrene flasks. A range of initial pH ($pH_{initial}$) values of the NaCl solutions and 50 mg of (2H/1 T) MoS_2 is adjusted from 2 to 12 by using 0.1 M of HCl and NaOH. The suspensions are shaken in a shaker and allowed to equilibrate for 24 h. The suspensions are then centrifuged at 5000 rpm for 15 min and the final pH (pH_{final}) values of the supernatant liquid are recorded. The value of pH_{ZPC} is the point where the curve of ($pH_{final} - pH_{initial}$) versus $pH_{initial}$ crosses the line equal to zero.

Acute toxicity assay

The acute toxicity level and effective concentration (EC_{50}) of the synthesized molybdenum disulfide (MoS_2) nanosheets are examined using a 2% screening test of Microtox Analyzer 500 (Modern Water Inc., USA). Five concentrations of MoS_2 nanosheets (50, 100, 250, 500, and 1000 µg. mL^{-1}) are toxicity tested. The tube containing 500 µL of diluent is inoculated with 10 µL of the resuspended bioluminescence *Vibrio fischeri* bacterium and used as a control, while in another test tube, 10 µL of each concentration of MoS_2 nanosheets and 10 µL of *Vibrio fischeri* are added to a tube containing 500 µL of diluent. The toxicity level and effective concentration (EC_{50}) are determined within 15 min.

Antimicrobial assay of (1 T/2H) MoS_2 nanosheets using disc diffusion method

In vitro antimicrobial effects for the five MoS_2 nanomaterial concentrations (50, 100, 250, 500, and 1000 µg. mL^{-1}) are tested. Six pathogenic microorganisms, including *Escherichia coli* O157:H7 (ATCC 35,150) and *Pseudomonas aeruginosa* (ATCC 10,145) as Gram-negative bacteria; *Listeria monocytogenes* (ATCC 25,152), *Staphylococcus aureus* (ATCC 43,300), and *Enterococcus faecalis* (ATCC 43,845) as Gram-positive bacteria; and *Candida albicans* (ATCC 10,231) as a yeast model, are involved in this assay. One hundred microliters of each refreshed pathogen is spread on the surface of Müller-Hinton agar plates (BBL, Germany). Sterile filter paper discs (6 mm in diameter) are saturated with MoS_2 nanosheets, and after that, the discs are placed on the surface of Müller-Hinton agar plates. The plates are incubated for 24 h at 37 °C. The diameters of inhibition zones were are measured in millimeters (mm) using a measuring ruler, whereas 6 mm in diameter means that the tested material has no antimicrobial effects [34, 35].

Disinfection effects of (IT/2H) MoS_2 nanosheets against pathogenic microorganisms

E. coli O157:H7, *Listeria monocytogenes*, and *Candida albicans* are used in this experiment. These preserved pathogens with 10% glycerol in − 20 °C are refreshed in 10-mL tryptic soy broth tubes (Merck, Germany). The inoculated tubes are incubated at 37 °C for 24–48 h. The grown microbial pathogens are centrifuged at 5000 rpm for 20 min and washed three times to remove any nutrients and/or debris. Preparation of the microbial pathogens is carried out 24 h before each experiment to determine the initial pathogenic counts, according to APHA (2017). Appropriate microbial counts ~ 10^6–10^7 CFU.ml^{-1} from each pathogen are separately inoculated into five tubes, of which each tube contains 10 mL from 50, 100, 250, 500, and 1000 µg. mL^{-1} of MoS_2 nanosheet suspension. The tubes are incubated in the lab temperature and under shaking at 150 rpm. The samples are withdrawn after different contact times (0, 15, 30, 45, 60, and 120 min). The pathogenic counts are determined using the pour plate method according to APHA (2017). The colonies are expressed as a colony-forming unit (CFU.ml^{-1}). The following equation is used to calculate the removal efficiency:

$$\textit{The removal efficiency}\ (R\%) = \frac{Ci - Co}{Ci} \times 100 \qquad (4)$$

where C_i is the initial pathogen counts at 0 min and C_o is the pathogen counts after exposure to MoS_2 nanosheets.

Results and discussion

The synthesis of mixed-phase 1 T/2H-MoS_2 nanosheets is conducted by a simple hydrothermal method. The pattern 2H-MoS_2 nanosheets are achieved by a commonly used hydrothermal process. During the formation of the 2H MoS_2 phase, the sulfur vacancies are formed because of the generated hot temperature as the induction factor [32]. The existence of sulfur vacancy changed the density of the surrounding electron cloud, which causes movement Mo to form a 1 T configuration, and finally, build up the mixed coexistence structure of mixed-phase 1 T/2H-MoS_2.

Morphological analysis

SEM and EDX measurements

The representative SEM images and EDX data of obtained sample are shown in Fig. S1a and b. It is shown that the sample has nanosheets layered structure (as the arrow shown in Fig. S1a) with typical

small holes on the surface which can act as active adsorption sites that are beneficial to catalytic activity. These folded nanostructures can significantly decrease the surface recombination of the photogenerated electrons and holes and improve the efficiency of collection, transfer, and separation of carriers, which is essential for enhancing photocatalytic activity.

Figure S1b shows the EDX spectrum of the sample; only sulfur and molybdenum atoms are detected besides the O_2 which comes from the alcohol used in measurement without any additional peak for impurities. This confirms that nanosheets contain only molybdenum and sulfur elements. Table S1 also demonstrates that the atomic ratio of Mo and S is 58.28% and 28.29%, which confirms that the product is MoS_2.

The morphology and nanostructure of the (1T/2H) MoS2 nanosheets are detected by transmission electron microscope (TEM), high-resolution Transmission Electron Microscope (HRTEM), and selected area electron diffraction (SAED) to obtain more insight into the crystal structure of the as-prepared (1T/2H) MoS2 nanosheets (Fig. S2 (a, b, c, d.)) Figure S2a and b reveal that the synthesized (1 T/2H) MoS_2 has consisted of multilayered layers of nanosheets. From the HTEM image it is found that the MOS2 nanosheets are stacked densely with clear lattice fringes with an interlayer spacing of 0.62 nm which suggesting the high crystallinity of the 2D networks (Fig. S2(c)). The selected area electron diffraction pattern (SAED) is illustrated in Fig. S2d, the visible diffraction rings could be indexed to (100) and (110) planes of the hexagonal [27]. The SAED pattern illustrates the crystalline nature of the 2D MoS_2, with highly diffused bands (Fig. S2d).

Structural analysis

The phase purity and crystal structure of (2H/1 T) MoS_2 nanosheets are considered by X-ray diffraction (XRD). As illustrated in Fig. 2a, the XRD spectra pattern of (2H/1 T) MoS_2 nanosheets shows crystalline with hexagonal crystal structure without any impurities. All the diffraction peaks are assigned to MoS_2's hexagonal phase and are compatible with the typical powder diffraction pattern (JCPDS No. 00–024-0513) [32, 36, 37]. Four characteristic diffraction peaks at $2\theta = 15.8°$, 32.8°, 39.5°, and 58.3° are expected for the (002), (100), (103), and (110) planes of typical 2H-MoS_2; on the other hand, the characteristic peaks of the 1 T phase are not easy to find, most likely as a consequence of the typical peaks of 1 T-MoS_2 being nearly the same as that of 2H-MoS_2 [32, 38]. The broader nature of this diffraction peak indicates the presence of layered MoS_2 with a lamellar structure of very small size [39]. The relative intensities of the diffraction rings are consistent with the TEM result. The average crystallite sizes of the prepared (2H/1T) MoS2 nanosheets are determined from (002) diffraction peaks in the XRD patterns using the Scherer equation (Eq. 5) [40–42].

$$D = \frac{K\lambda}{\beta Cos\theta} \tag{5}$$

where K is the shape factor (0.9), λ is the wavelength of Cu radiation (1.5406 Å), and β is the Bragg diffraction angle. The calculated crystallite size of the (2H/1 T) MoS_2 nanosheets are found to be 1.7 nm**.** In addition, according to Bragg's equation, the d-spacing for the (002) plane in the (2H/1 T) MoS_2 is calculated to be 0.62 nm. This (002) d-spacing value for the crystalline plane of the MoS_2 is consistent with the interlayer distance obtained from the TEM results (Fig. S2).

Raman scattering analysis is one of the most essential techniques to characterize the 2D materials to confirm their formation and analysis of their phase and composition. Figure 2b illustrates the broad region Raman profiles for phase (2H/1 T) MoS_2 nanosheets ranging from 100 to 1000 cm^{-1}. The Raman test of (2H/1 T) MoS_2 should present two kinds of optical phonon modes ($E^1{}_{2g}$ and A_{1g}) which represent two distinguished peaks in the MoS_2 spectrum, where $E^1{}_{2g}$ is the vibrational modes inside layers (in-plane sulfur-molybdenum vibrations) by the two S atoms with opposite vibration to the Mo atom, and A_{1g} corresponds to the movements of complete layers (out-plane sulfur vibrations) by the vibration of two S atoms toward opposite directions with Mo atom stationary. As illustrated in Fig. 2b, the Raman spectra of (2H/1 T) MoS_2 nanosheets display peaks around 283 cm^{-1} and 378 cm^{-1} which can be assigned to the E_{1g} and $E^1{}_{2g}$ vibration modes, respectively, while the peak at 415 cm^{-1} is assigned to A_{1g} vibration mode. In the out-of-plane A_{1g} mode, the restoring force is primarily due to interlayer van der Waals interaction [43, 44]. These four peaks are corresponding to the 2H-MoS_2. From the

spectrum, it can be found that, based on the original three peaks, there are two peaks at 215 cm^{-1} and 338 cm^{-1}, respectively, which are coincided with the 1 T phase MoS_2. These peaks are essentially resulting from the changes in the structure of the material itself. It can be concluded that there is an optimal structure with coexisting 2H and 1 T phases of the MoS_2 nanosheets and the structural phase is a mixed 2H/1 T phase [43, 44]. We can also observe three additional bands at 668, 821, and 995 cm^{-1} in the Raman spectra of (2H/1 T) MoS_2 nanosheets [33]. These bands represent MoO_3 vibrational energy states as a result of oxidation by laser irradiation [32, 45].

Optical properties

One of the most significant features to identify the optical property of a semiconductor is its absorption. Figure 2c and d illustrate the UV–vis diffuse reflectance absorption spectrum of (2H/1 T) MoS_2 nanosheets. The as-synthesized MoS_2 nanosheets show total absorption in the examined spectral region, with strong absorption in the UV range with a maximum at 270 nm, which is very similar to that of MoS_2 nanoparticles reported by [46–48], denoting its respective visible light response. Figure 2d depicts how the curve of $(\alpha hv)^{1/2}$ varies with photon energy. The tangent intercept indicates the (2H/1 T) MoS_2 nanosheets' bandgap value, which is found to be 1.17 eV.

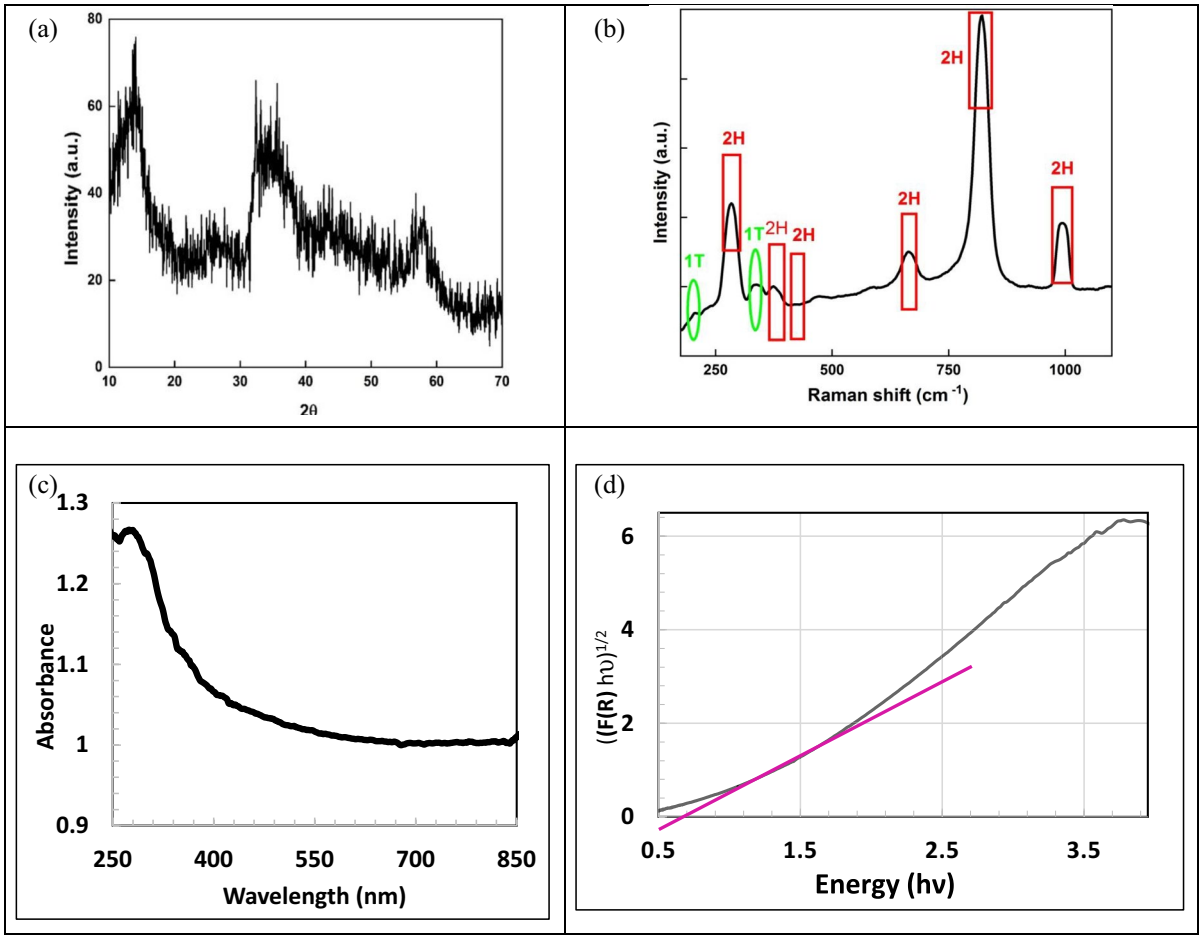

Fig. 2 **a** The XRD pattern of the prepared (2H/1 T) MoS_2 nanosheets. **b** Raman spectrum for the prepared (2H/1 T) MoS_2 nanosheets. **c** Optical characteristics of the (2H/1 T) MoS_2 nanosheets (diffuse reflectance spectra in the UV–vis range). **d** Bandgap estimation of synthesized MoS_2 nanosheets by plots of $((F(R)\ hu)^{1/2}$ against E g photon energy

Surface area

For heterogeneous reactions, the specific surface area is proportional to the number of catalytically active centers [49]. Therefore, this is an important parameter of the photocatalytic activity of the synthesized sample. The specific area of the as-prepared (2H/1 T) MoS_2 is determined by the Brunauer–Emmett–Teller (BET) analysis [42]. The specific surface area (SBET), pore size, pore radius D v(r), and the total pore volume (V_p) of the as-prepared (2H/1 T) MoS_2 nanosheets have been measured to be 1340 $m^2\ g^{-1}$, 3.1 nm, 1.93 nm, and 0.089 $cc.g^{-1}$, respectively.

Adsorption and reduction activity of hexavalent chromium ions (Cr^{6+})

The adsorption experiment is an important step for Cr^{6+} reduction. The adsorption experiment is performed at different times with an initial concentration of 20 ppm, a catalyst dose of 0.2 g. L^{-1}, and at pH 3 as revealed in Fig. 3. It is found that the adsorption of MoS_2 nanosheets of Cr^{6+} is 77%, 84%, and 100% for reaction times of 5, 10, and 15 min, respectively. After reaching the adsorption–desorption equilibrium, a filtered sample is taken, and the Cr^{6+} ion concentration is measured by a UV–vis spectrophotometer and with using the colorimetric method. It can be concluded that the Cr^{6+} concentration in the reaction solution is zero which confirmed that all Cr^{6+} ions are adsorbed on the (2H/1 T) MoS_2 nanosheet's surface.

Then the solution for the photoreduction step (under solar simulator) has been taken. A filtered sample is taken at interval times and it is observed that Cr^{+6} concentration is still zero. It is established that the reduction of Cr^{6+} to Cr^{3+} under solar radiation begins at the same time as the desorption of Cr^{+6} from the catalyst surface. This is evidenced by the fact that, in the beginning, all the Cr^{6+} is adsorbed on the catalyst surface (Cr^{6+} concentration is zero in the solution). Once the solar simulator is turned on and the photoreduction process starts, the Cr^{6+} starts to reduce to Cr^{3+} on the MoS_2 nanosheets and desorbed in the solution. The Cr^{3+} concentration can be calculated by measuring the Cr (total) according to Eq. 1. Figure 3b demonstrates the increase in Cr^{3+} concentration with increasing the reduction time which returns to 20 ppm after 90 min. In addition, the Cr^{6+} concentration remains zero (Fig. 3b).

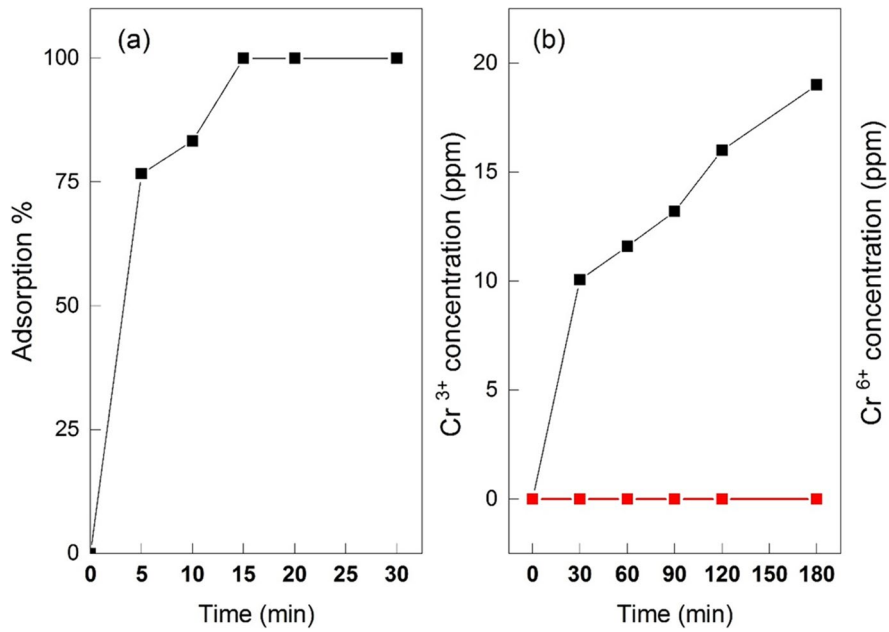

Fig. 3 **a** Adsorption % and **b** photoreduction % of (2H/1 T) MoS_2 nanosheets at initial concentration of 20 ppm, 0.2 g. $L.^{-1}$ catalyst dose, pH 3

Adsorption isotherm

To understand the mechanism of chromium adsorption and adsorption properties and interactions, adsorption isotherms of $Cr_2O_7^{2-}$ solutions with different initial concentrations from 10 to 80 ppm at pH 3 are applied (Fig. 4a, b) [49, 50]. Both the Langmuir and Freundlich models are used to further quantify the experimental adsorption data and evaluate the adsorption capacity and the adsorbent affinity for the heavy metal ions [51]. Their linear equations (Eqs. 6, 7) are as follows:

$$\frac{c_e}{q_e} = \frac{c_e}{q_{max}} + \frac{1}{k_L q_{max}} \tag{6}$$

$$lnq_e = lnk_F + \frac{lnc_e}{n} \tag{7}$$

where q_{max} (mg g^{-1}) is the Langmuir maximum adsorption capacity necessary to form a monolayer on the adsorbent surface, c_e (mg L^{-1}) denotes the equilibrium concentration of the solution, K_L (L mg^{-1}) and K_F (mg g^{-1}) represent the Langmuir and Freundlich

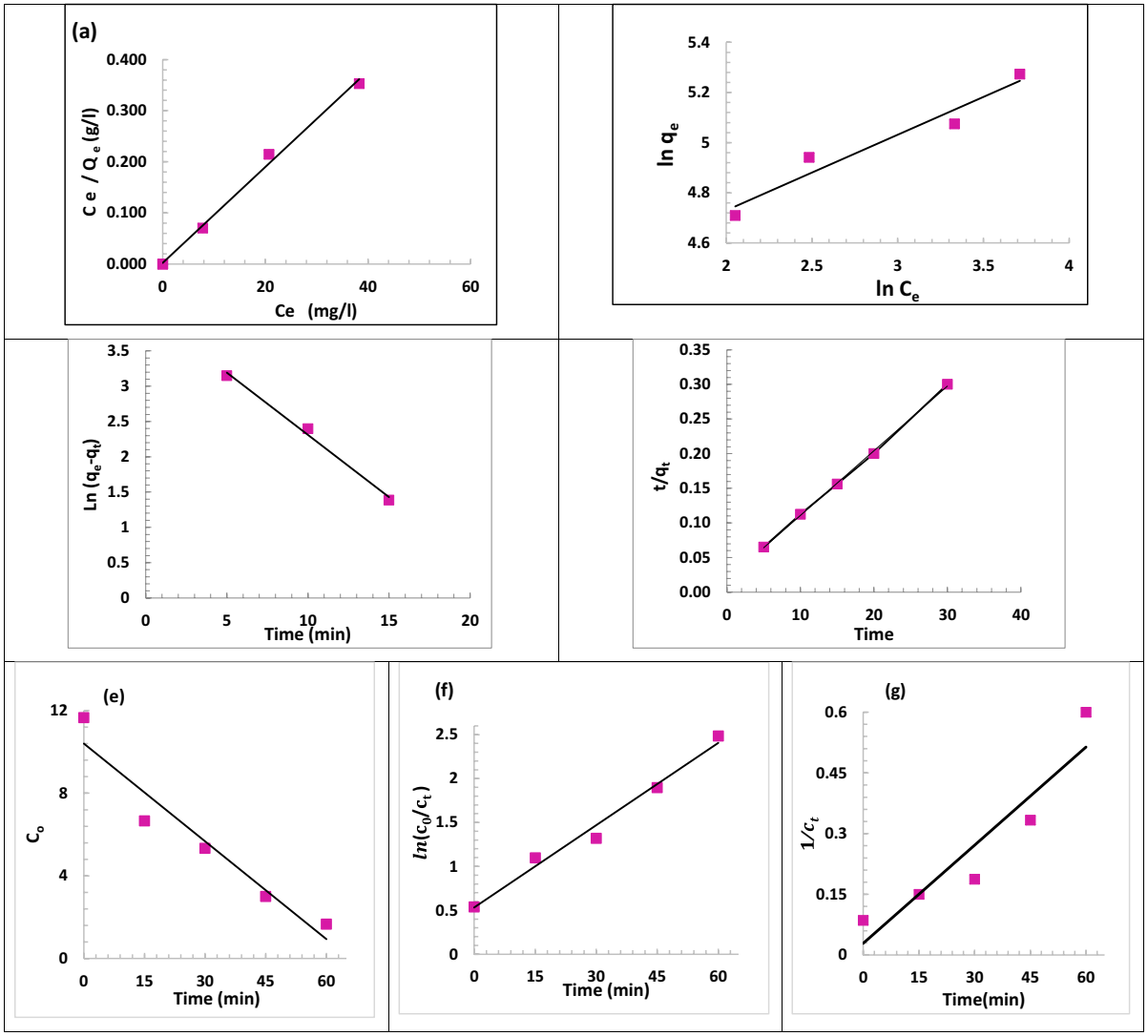

Fig. 4 Adsorption **a** Langmuir and **b** Freundlich model fitting plot (initial concentration of Cr^{6+}: 10–80 mg L^{-1}; absorbent dosage: 0.2 g L^{-1}; initial solution pH: 3; equilibrium time: 30 min). **c** Pseudo-first-order and **d** second-order adsorption kinetic fitting plots (30 ppm catalyst dose: 0.2 g L^{-1}; solution pH: 3). **e** Pseudo-zero-order, **f** first-order, and **g** second-order photoreduction kinetic fitting plots (catalyst dose: 0.2 g $L.^{-1}$; solution pH: 3)

constants, respectively, and n is an empirical parameter related to the intensity of adsorption. Table S2 shows the values of the linear regression coefficients (R^2) as well as the equivalent calculated parameters (q_{max}, K_L, K_F, and n). The validity of each model is checked using the correlation coefficient. It is worth observing that applying the Langmuir adsorption isotherm model gives a higher correlation coefficient with a maximum adsorption capacity (q_{max}) of 106.5 mg g^{-1} as illustrated in Table S2. It can be concluded that the Langmuir model is suitable for explaining the adsorption of chromium (Fig. 4a). As a result, chromium adsorption on the homogenous surface of MoS_2 is regarded as a single layer [52]. Furthermore, the plot of the Freundlich model is illustrated in Fig. 4b. Table S2 shows the adsorption capacity at a unit concentration (K_F) and the adsorption intensity (1/n). The 1/n value of 0.3 indicates that the adsorption process is favorable.

The kinetics of the adsorption

The data is fitted to various kinetic models, including pseudo-first and second-order models (Fig. 4c, d), to explore the kinetics of the adsorption process (Eqs. 8, 9). Such models provide precise information on the adsorption mechanism as well as the types of adsorption processes that are involved, such as diffusion control, chemical reaction, and mass transport processes.

$$In\left(q_e - q_t\right) = Inq - k_1 t \tag{8}$$

$$\frac{t}{q_t} = \frac{t}{q_e} + \frac{1}{k_e q_e^2} \tag{9}$$

where the pseudo-first and pseudo-second-order rate constants are K_1 and K_2, respectively (g mg^{-1} min^{-1}). The amounts adsorbed at time t and equilibrium (mg g^{-1}) are given by q_t and q_e, respectively.

The pseudo-first-order did not provide an acceptable fit for the experimental data, as seen in Fig. 3c, even though R^2 is 0.992 but the q_e is 59 mg g^{-1} for 20 mg L^{-1} dye, which is significantly lower than the experimental value of q_e (100 mg g^{-1}). As shown in Fig. 4d, the pseudo-second model as well shows a good-order correlation. Furthermore, the obtained q_e values (e.g., 107 mg g^{-1}, Table S2) are significantly close to the experimental value (100 mg. g^{-1}). These results suggest that the adsorption process is highly dependent on the surface-active sites created by MoS_2 nanosheet interfaces.

The adsorption process of hexavalent chromium ions on the surface of (2H/1 T) MoS_2 nanosheets is likely to be dominated by chemisorption, suggesting that the overall rate of the nanosheet adsorption process is controlled by intraparticle diffusion and the boundary layer diffusion by [53].

Photoreduction kinetics

As is well known, the process of reduction depends on several factors such as mass transfer, diffusion rate control, and chemical reactions [50, 54]. To understand the mechanism of chromium reduction, the fitting of experimental data with the models of pseudo-zero order, first-order kinetic model, and pseudo-second-order kinetic is investigated that can be described using the following equations (Eqs. 10, 11, 12), respectively:

$$C_t = C_0 - k_0 t, t_{1/2} = \frac{c_0}{2k_0} \tag{10}$$

$$\mathrm{In[C_t]} = \mathrm{In[C_0]} - K_1\ \mathrm{t}, \mathrm{t}_{1/2} = \frac{\mathrm{ln}\ 2}{\mathrm{K_1}} \tag{11}$$

$$\frac{1}{\mathrm{c_t}} = \frac{1}{\mathrm{c_o}} + \mathrm{k_2 t}, \mathrm{t}_{1/2} = \frac{1}{\mathrm{c_0 k_2}} \tag{12}$$

where C_0 and C_t are the initial metal concentration and concentration at time t respectively; k_0, k_1, and k_2 are the rate constants of the zero-, first-, and second-order kinetics, respectively.

The rate constant and the corresponding correlation coefficient R^2 are calculated from the graphs of the three models (Fig. 4e, f, g). According to the R^2 value, it can predict the equation that fits the experimental data. The half-life time ($t_{1/2}$) from each equation has been calculated and compared with the experimental one. The values of the parameters and the correlation coefficients obtained from these three kinetic models have been accumulated in Table S2. In conclusion, the pseudo-first-order model is the most suitable for describing the reduction process, as evidenced by its higher correlation coefficient.

In addition, the photoreduction rate constant (k_1) is calculated to be 0.031 and the calculated $t_{1/2}$ is 22 min, which is closed to the experimental ones. This confirms that the first-order kinetic model is a model that describes photocatalytic reduction.

Effect of (2H/1 T) MoS_2 nanosheet doses on adsorption efficiency

Among the various variables that affect adsorption, the doses of MoS_2 nanosheets are a particularly important factor due to their cost estimation per unit of solution price. The percentage of Cr^{6+} ion adsorption from an aqueous medium as a function of the (2H/1 T) MoS_2 nanosheet doses of 0.1, 0.2, 0.25, and 0.4 g. L^{-1} at solution pH value of 3 is shown in Fig. 5a. It is found that increasing the dose amount of MoS_2 catalyst leads to an increase in the adsorption percentage. After 15 min, the adsorption percentage obtained with 0.1 g. L^{-1} dose is 34%. Although with doses of 0.2, 0.25, or 0.4 g L^{-1}, the adsorption percent reached 100%, the adsorption percentage for a 0.1 g. L^{-1} dose reaches 100% after 30 min, as shown in Fig. 5a.

The improvement in Cr^{6+} adsorption efficiency is thought to be due to the unique structure of (2H/1 T) MoS_2 nanosheets. The defects on the surface of the nanosheet provide penetrable channels for Cr^{6+} ion diffusion. In addition, the high surface area of (2H/1 T) MoS_2 nanosheets and the availability of active sites on their surface facilitate the interaction and are beneficial for the transport of Cr^{6+} from its bulk solution to the active site on nanosheets [51, 54, 55].

Effect of doses on photoreduction activity

The comparative process for the different (2H/1 T) MoS_2 nanosheet doses used for Cr^{6+} photoreduction under a solar simulator is shown in Fig. 5b. It is found that the photoreduction process is enhanced as well as the Cr^{3+} concentration in the solution increases with increasing the catalyst dose from 0.1 to 0.4 g L^{-1} [55]. In addition, at a constant MoS_2 dose, the Cr^{3+} concentration increases with increasing contact time. It is found that, with 0.25 and 0.4 g. L^{-1} doses, the Cr^{3+} concentration retains to 20 ppm after 2 h. This proves that all the Cr^{6+} is reduced to Cr^{3+}.

Effects of the initial pH level on Cr (VI) adsorption

Solution pH is an important and controllable parameter that can affect the surface charge, the degree of protonation of the adsorbent, and the degree of ionization of the adsorbate [31]. It can play a key role in the adsorption and photocatalytic reduction efficiency of Cr^{6+} [55].

The influence of solution pH on the adsorption efficiency is carried out by adjusting the pH of the initial solution in the range of 2.0–7.0, in which the initial Cr^{6+} concentration is kept at 20 ppm with 0.2 g. L^{-1} catalyst dose. The variation of the Cr^{6+} adsorption % at different pH levels is shown in Fig. 5c. It can be shown that, as the solution pH increases up to 3, the percentage of Cr^{6+} adsorption % increases. Beyond this value, a sharp decrease is observed in the adsorption %. After 15 min under acidic conditions of pH 2 and pH 3, 75% and 100% Cr^{6+} are adsorbed on (2H/1 T) MoS_2 nanosheets, respectively. When the pH level is increased to pH 5 and pH 7, the Cr^{6+} adsorption % decreased to 64% and 28% respectively.

The reason why MoS_2 nanosheets perform differently in adsorbing Cr^{6+} at different pH values in the solution can be explained by considering the pH value of the point-of-zero charges (ZPC) [56]. The pH at the ZPC (pH_{ZPC}) of the (2H/1 T) MoS_2 nanosheet surface is important as it indicates the acidity/basicity and the net surface charge in the solution.

As shown in Fig. 5d, the pH_{ZPC} of (2H/1 T) MoS_2 nanosheets is 2.6; this means that its surface is positively charged at a solution pH value below 2.6. As below 2.6, the Cr^{6+} in aqueous solution is found to be in the forms of $HCrO_4^-$ and $Cr_2O_7^{2-}$ and $HCrO_4^-$ is the main species [31]. So, the high adsorption % at low pH is mainly due to the electrostatic interaction between the anionic forms of Cr^{6+} and the surface of MoS_2 with positive charges via high protonation.

When the pH is raised to pH 5, the MoS_2 surface is negatively charged but not high enough, and its coulomb repulsive interaction with Cr^{6+} is not strong enough; thus, it shows moderate adsorption (65%). With increasing the solution pH to 7, the MoS_2 negatively charged surface increased. Also, Cr^{6+} is gradually shifted to the form of CrO_4^{2-} species which has a highly negatively charged surface. Consequently, this strengthened the electrostatic repulsion between (2H/1 T) MoS_2 nanosheets and Cr^{6+}, making Cr^{6+} adsorption more difficult. It can be concluded that $HCrO_4^-$ is better adsorbed than CrO_4^{-2} due to its lower free adsorption energy [57].

On the other hand, increasing the pH value increases the concentration of OH ions present in the solution. Therefore, there is competition between the Cr^{6+} species and OH ions on the surface of the M, which leads to a decrease in the adsorption efficiency.

Effects of the initial pH level on Cr^{6+} photoreduction efficiency

Figure 5e depicts the concentration variations of different Cr ion species including Cr^{6+} and Cr^{3+} in aqueous solutions over contact time at different pH during the reduction of Cr^{6+} using (2H/1 T) MoS_2 nanosheets. It is found that reduction in acidic solutions provides higher photoreduction efficiency than in alkaline solutions. The photoreduction efficiency decreased significantly with increasing pH. As shown in Fig. 5e, all Cr^{6+} ions are adsorbed on the (2H/1 T) MoS_2 surface at pH 2 and pH 3 so its concentration is zero, even though the Cr^{3+} concentration raised to a plateau due to the continuous reduction of the adsorbed Cr^{6+} on the surface to Cr^{3+}, which reached 100%. At pH 5, the concentrations of Cr^{6+} in the solution decreased slightly, whereas the Cr^{3+} concentration increased initially to reach a plateau. The Cr^{6+} reduction efficiency decreased to 35%. There is no photoreduction observed with pH 7 (Fig. 5e).

The increased photoreduction potential at lower pH can be attributed to an increase in the thermodynamic driving force of electrons from CB to Cr^{6+} ions [57, 58]. In addition to the previously mentioned 100% adsorption capacity of Cr^{6+} on the MoS_2 surface, the reduction begins at the surface of MoS_2. Meanwhile, increasing the solution pH higher than 3, the driving force for the reduction of molecular oxygen is higher than for the Cr^{6+}, and as a result, O_2 may compete for the photogenerated electrons and decrease the rate of Cr^{6+} photoreduction [31, 51, 55].

The mechanism for removing Cr^{6+} ions over MoS_2 nanosheets is dependent on the synergistic effect of adsorption-photocatalysis. The photoreduction activity of (2H/1 T) MoS_2 nanosheets is highly dependent on interfacial reactions. For instance, the reduction of Cr^{6+} occurs under three stages, adsorption to the surface-active center, photoreduction, and surface desorption, as shown in Fig. 6. Firstly, Cr^{6+} should adsorb on the surface of (2H/1 T) MoS_2. Then, the photogenerated electrons move to the MoS_2 surface and react with Cr^{6+}. Based on the opposite charge properties of Cr^{6+} and Cr^{3+}, when Cr^{6+} is reduced to Cr^{3+}, Cr^{3+} is quickly removed or desorbed from the surface [31, 32]. So, it is vital to promote Cr^{6+} surface adsorption as well as Cr^{3+} repulsion to maximize the photoreduction performance.

FTIR measurements

The molecular structure and function groups of (2H/1 T) MoS_2 nanosheets, MoS_2 nanosheets adsorbed Cr^{6+}, and after photoreduction are identified using FTIR spectroscopy as revealed in Fig. 7a, b, c. From Fig. 7a for the pristine MoS_2 nanosheets, it should be noted that the peaks at 3398 cm^{-1}, 3138 cm^{-1}, and 1631 cm^{-1} are related to the bending and stretching vibrations of the hydroxyl group of adsorbed water molecules, respectively. The peaks at 1627 cm^{-1} and 1133 cm^{-1} are attributed to the stretching vibration of S–O in MoS_2 nanosheets [18]. The stretching vibration sharp peak of S-Mo-S is represented at 1403 cm^{-1}. However, the band of O–H bending can be found at 1052 cm^{-1}. The characteristic peaks for out-plane vibration of S atoms (S–S) appear at ~944 cm^{-1}. A peak at 905 cm^{-1} might be related to the asymmetric vibration of the Mo–O group. A peak of Mo-S stretching vibration mode is found at 597 cm^{-1}. The spectrum of chromium adsorbed MoS_2 also signifies that after being loaded with metal ions (Fig. 7b), the functional groups of MoS_2 are slightly affected in their position and intensity. These wavelength shifts illustrated that there is metal binding action taking place at the surface of the adsorbents [58] [59]. The clear shifts appear from 3398 cm^{-1} and 3138 cm^{-1} for MoS_2 to 3737 cm^{-1} and 3254 cm^{-1} for Cr-loaded MoS_2 respectively and with the appearance of a new peak at 2916 cm^{-1} which confirmed that the surface -OH group is one of the functional groups responsible for adsorption [60]. The S–O peak of MoS_2 is slightly shifted from 1133 cm^{-1} and 1627 cm^{-1} to 1126.22 cm^{-1} and 1631 cm^{-1}, indicating that the S-OH group is also responsible for adsorption [61]. The peak of Mo–O stretching vibration at 902 cm^{-1} shifted to 952 cm^{-1} which confirms that Mo–O is also responsible for adsorption. Figure 7c illustrates the FTIR spectrum after reduction, which confirmed that there is no change in (2H/1 T) MoS_2 structure after reduction with no observed peak for Cr^{6+} or Cr^{3+} on the (2H/1 T) MoS_2 surface.

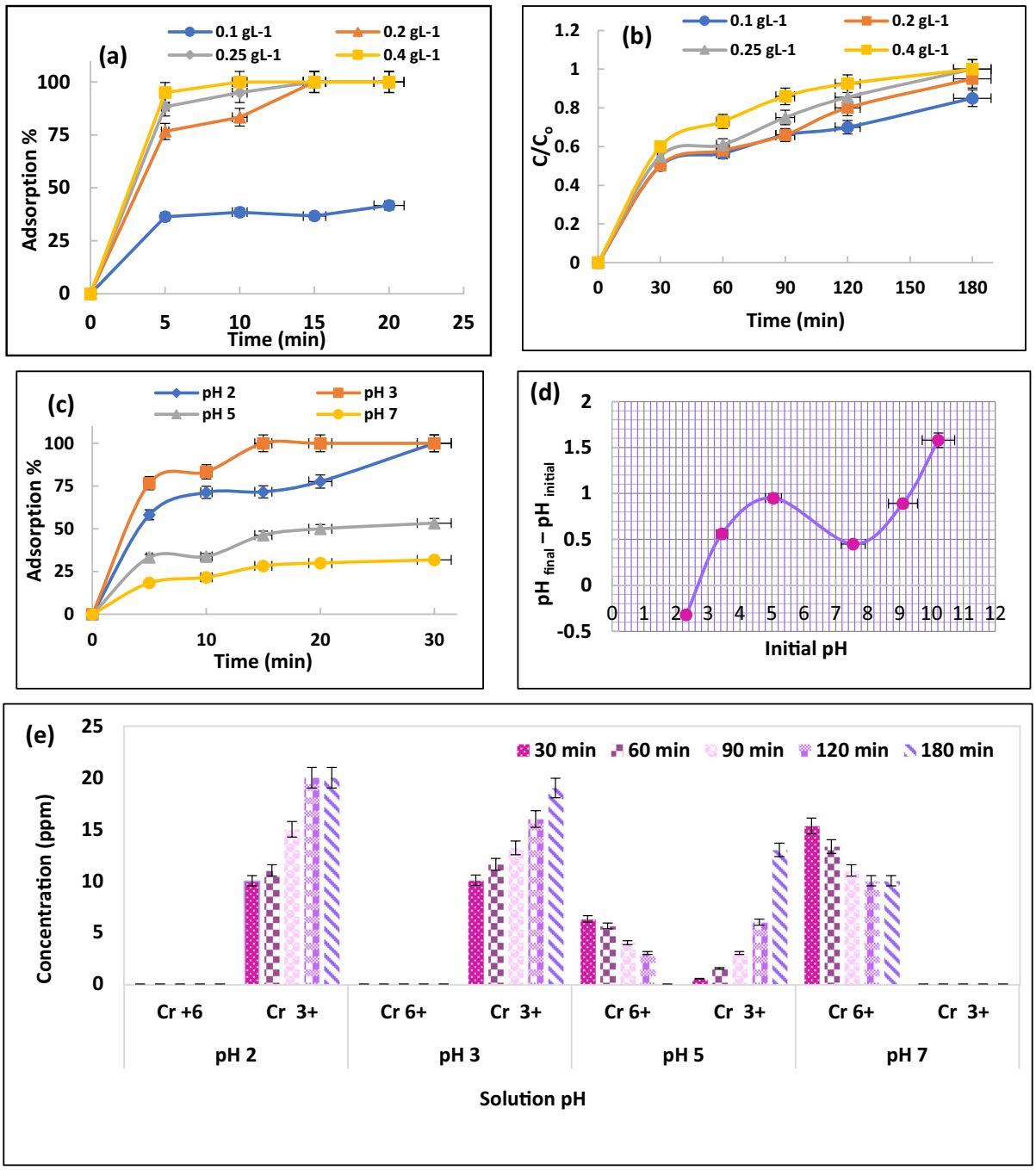

Fig. 5 **a** Effect of (2H/1 T) MoS_2 nanosheet dose on adsorption percent for Cr^{6+}. **b** Photoreduction of the adsorbed Cr^{6+} to Cr^{3+} for different (2H/1 T) MoS_2 nanosheet doses (initial Cr^{6+} concentration 20 ppm, solution pH 3). **c** Effect of solution pH on adsorption % for Cr^{6+} (initial concentration: 20 ppm; dose: 0.2 g. L^{-1}). **d** Determination of pH of zero-point charge, **e** the concentration variations of different Cr^{6+} ion species including Cr^{6+} and Cr^{3+} in aqueous solutions over contact time at different pH

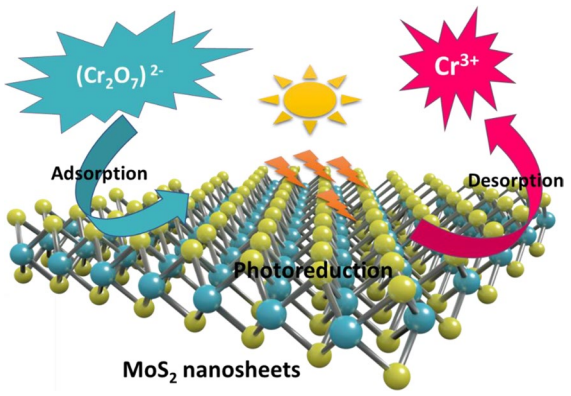

Fig. 6 The proposed process of photocatalytic reduction of $Cr.^{6+}$ on MoS_2 nanosheet surface (transfer after the studying removal)

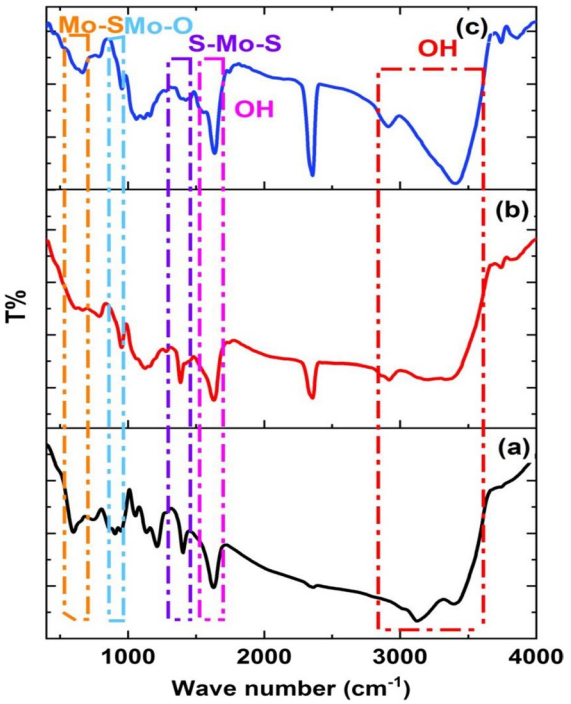

Fig. 7 Fourier transform infrared (FTIR) spectroscopy spectra of **a** MoS_2 nanosheets; **b** MoS_2 after Cr^{6+} adsorption; and **c** MoS_2 after Cr^{6+} reduction

Photocatalytic degradation of pharmaceutical compounds

Moreover, the activity of MoS_2 nanosheets is investigated for photodegradation of pharmaceutical pollutants (cefadroxil, cefotaxime, meloxicam, ibuprofen, and ciprofloxacin) from wastewater. Figure 8a illustrates the photodegradation of pharmaceuticals using sunlight-assisted photocatalysis with a MoS_2 dose of 0.2 g. L^{-1} in a natural pH (i.e., pH = 7). After 60 min, it is found that the obtained degradation rates are 100%, 95%, 90%, 80%, and 42% for cefadroxil, ciprofloxacin, meloxicam, cefotaxime, and ibuprofen, respectively. Moreover, the complete degradation of ciprofloxacin, meloxicam, and cefotaxime is achieved after 60, 90, and 90 min of sunlight irradiation respectively over MoS_2 nanosheets. Meanwhile, ibuprofen is completely removed after 120 min. The higher degradation rate of cefadroxil, meloxicam, ciprofloxacin, and cefotaxime is attributed to the higher polar surface of these molecules in aqueous, where the values of polar size are 13.3, 13.6, 7.45, and 17.35 nm according to drug banks. The great polar surface area has increased the capability of adsorption for these pharmaceuticals over the MoS_2 nanosheets, which leads to enhancing photocatalytic degradation. Also, the higher pKa values for cefadroxil (7.22), ciprofloxacin (6.3), and cefotaxime (9.84) increased adsorption of this pharmaceutical which is inconsistent with the photodegradation rates. Meanwhile, ibuprofen has a lower polar surface area (3.73 nm) and pKa (4.43) value in an aqueous solution which leads to a decrease in the adsorption affinity over MoS_2 nanosheets and results in a decline in the photodegradation rate. The photodegradation of pharmaceuticals is found to be fitted with pseudo-first-order (PFO) as shown in Fig. 8b. Furthermore, the PFO rate constants are calculated for the degradation of pharmaceutical pollutants and are illustrated in Fig. 8c. The PFO rate constants are found to be 0.014, 0.0268, 0.0384, 0.0463, and 0.0994 min^{-1} for ibuprofen, cefotaxime, meloxicam, ciprofloxacin, and cefadroxil respectively. The PFO rate constant of cefadroxil is 7.1, 3.7, 2.6, and 2.15 times higher than that of ibuprofen, cefotaxime, meloxicam, and ciprofloxacin, respectively. Likewise, the normalized initial rates of degradation per catalyst dose of pharmaceuticals are calculated and the value is 1.4, 2.68, 3.84, 4.63, and 9.94 mg. L^{-1}. $min^{-1}.g^{-1}$ for ibuprofen, cefotaxime, meloxicam, ciprofloxacin, and cefadroxil, respectively. Conclusively, the hydrothermal MoS_2 nanosheets are a non-selective proficient photocatalyst for the decontamination of pharmaceutical pollutants.

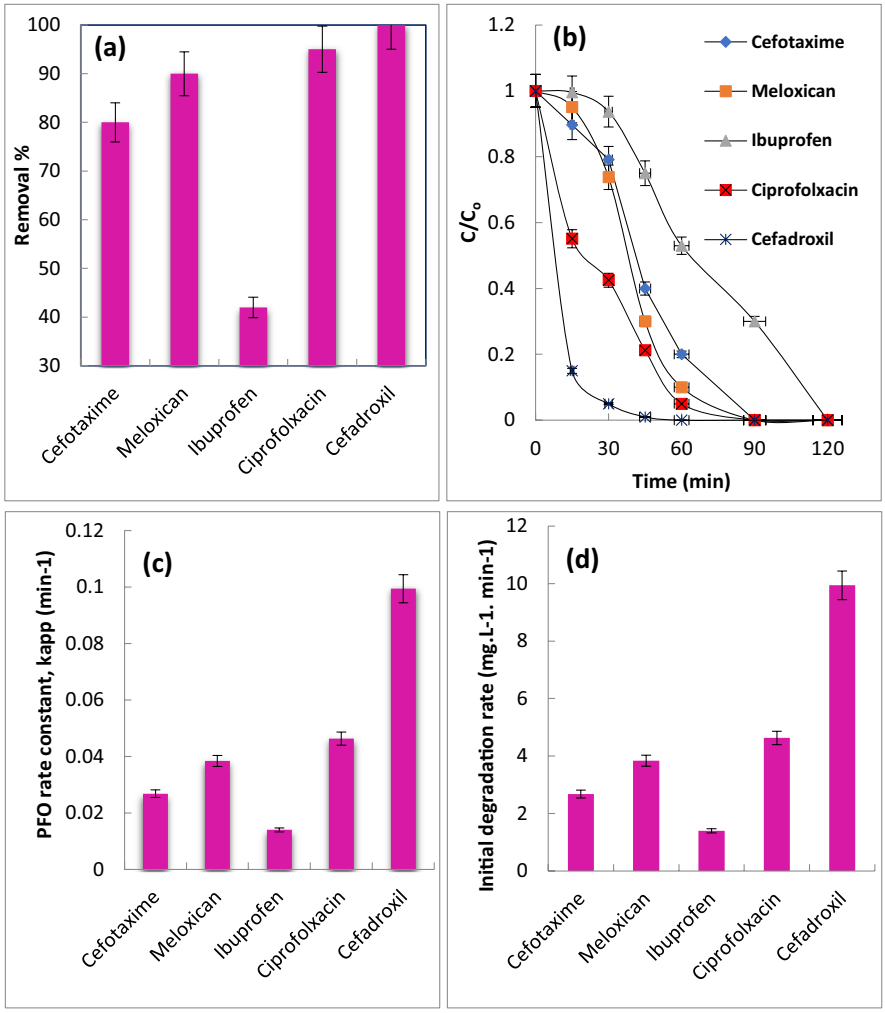

Fig. 8 **a** Photocatalytic degradation of different pharmaceuticals over (2H/1 T) MoS_2 nanosheets, **b** removal % pseudo-first-order (PFO) kinetic of different pharmaceuticals. **c** PFO rate constant, **d** initial degradation rate of pharmaceutical

Toxicity results

Any materials that will be introduced to the environment should be checked for their safety and toxicity [62]. The toxicity result showed that 1000 µg. mL^{-1} of molybdenum disulfide (MoS_2) nanosheets has a slightly toxic effect and EC_{50} was 93, while the concentrations of 500, 250, 100, and 50 µL/mL of MoS_2 exhibit any toxicity toward bioluminescence *Vibrio fischeri* bacterium (Table 1). Some studies showed that 10 mg.L^{-1} of MoS_2 exhibits toxicity against organisms such as zebrafish and algae [63, 64]. Teo et al. (2014) [65] found that MoS_2 nanosheets have low in vitro cytotoxicity against the A549 human cell line at high concentrations after 24 h.

Antimicrobial assay of MoS_2 using disc diffusion method

All the tested MoS_2 concentrations have an antimicrobial effect against the tested pathogenic microorganisms (Fig. 9). Table 2 demonstrates that the highest antimicrobial effect is shown against *E. coli* O157:H7 with 12 mm through concentrations from 250 to 1000 µg. mL^{-1}. On the other hand, the lowest antimicrobial effect is shown against *Candida albicans* with 9 mm through concentrations from 50 to 500 µg. mL^{-1}.

Table 1 The acute toxicity levels and EC_{50} of the different concentrations of the prepared MoS_2 with reference ranges

Material	Toxicity results		Reference ranges	
	EC_{50}	Toxicity level	EC_{50}	Toxicity level
1000 µg. mL^{-1}	93	Slightly toxic	≥ 100	Non-toxic
500 µg. mL^{-1}	102	Non-toxic	60–99	Slightly toxic
250 µg. mL^{-1}	135	Non-toxic	40–59	Moderately toxic
100 µg. mL^{-1}	148	Non-toxic	20–39	Very toxic
50 µg. mL^{-1}	160	Non-toxic	0–19	Extremely toxic

Disinfection effects of MoS_2 nanosheets against pathogenic microorganisms

The results showed that the five concentrations (50, 100, 250, 500, and 1000 µg. mL^{-1}) of molybdenum disulfide (MoS_2) nanosheets have disinfectant effects against the three tested pathogenic microbes (*E. coli* O157:H7, *Listeria monocytogenes*, and *Candida albicans*). The removal efficiency (R %) of the tested pathogens is increased by MoS_2 concentrations and contact time increase (Figs. 10, 11, and 12). Approximately 88 and 97% of *E. coli* O157:H7 are deactivated using 50 and 100 µg.mL^{-1} of MoS_2 nanosheets after 120-min contact time (Fig. 10a, b), whereas complete removal (100%) of *E. coli* O157:H7 is observed with 1000, 500, and 250 µg.mL^{-1} of MoS_2 after contact times 30, 45, and 45 min, respectively (Fig. 10c, d, e). On the other hand, 86 and 96% of *Listeria monocytogenes* have been removed with 50 and 100 µg.mL^{-1} of MoS_2 after 120 min as a contact time (Fig. 11a, b). Moreover, complete inactivation for *Listeria monocytogenes* is shown with 1000, 500, and 250 µg.mL^{-1} of MoS_2 nanosheets after contact times 30, 45, and 60 min (Fig. 11c, d, e). The results concluded that *Listeria oncogenes* slightly response to MoS_2 nanosheets (when using 50 and 100 µg.mL^{-1}) in comparison with *E. coli* O157:H7. This may be due to *E. coli* as a Gram-negative bacterium having a thin peptidoglycan layer (7–8 nm) in its cell wall, while *Listeria monocytogenes* as a Gram-positive bacterium has a thick peptidoglycan layer that nanoparticles do not easily enter to the cytoplasm [66]. Figure 12 illustrates that about

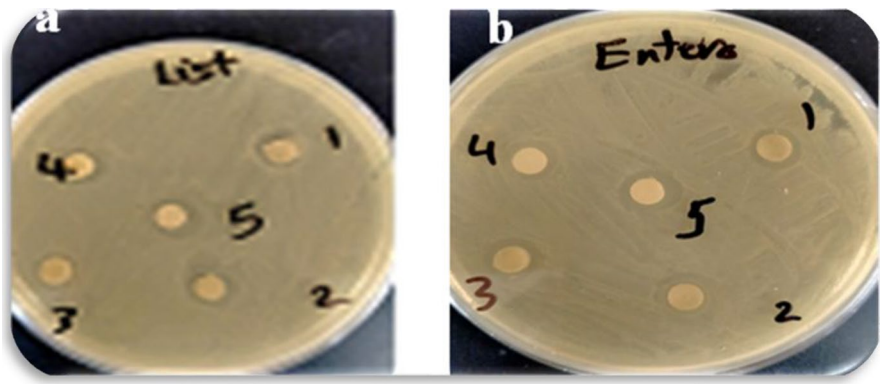

Fig. 9 Antimicrobial effect of MoS_2 against **a** *Listeria monocytogenes* and **b** *Enterococcus faecalis*; disc 1 saturated by 1000 µg. mL^{-1}, disc 2 saturated by 500 µg. mL^{-1}, disc 3 saturated by 250 µg. mL^{-1}, disc 4 saturated by 100 µg. mL^{-1}, and disc 5 saturated by 50 µg. $mL.^{-1}$

Table 2 Antimicrobial effect of different MoS_2 nanosheet concentrations against pathogenic microorganisms

MoS_2 concentration	Inhibition zone diameters (mm)					
	E. coli O157:H7	*Pseudomonas aeruginosa*	*Listeria monocytogenes*	*S. aureus*	*Enterococcus faecalis*	*C. A*
1000 µg. mL^{-1}	12	10	10	10	10	10
500 µg. mL^{-1}	12	10	10	10	10	9
250 µg. mL^{-1}	12	10	10	10	10	9
100 µg. mL^{-1}	11	10	10	10	10	9
50 µg. mL^{-1}	11	10	10	10	10	9

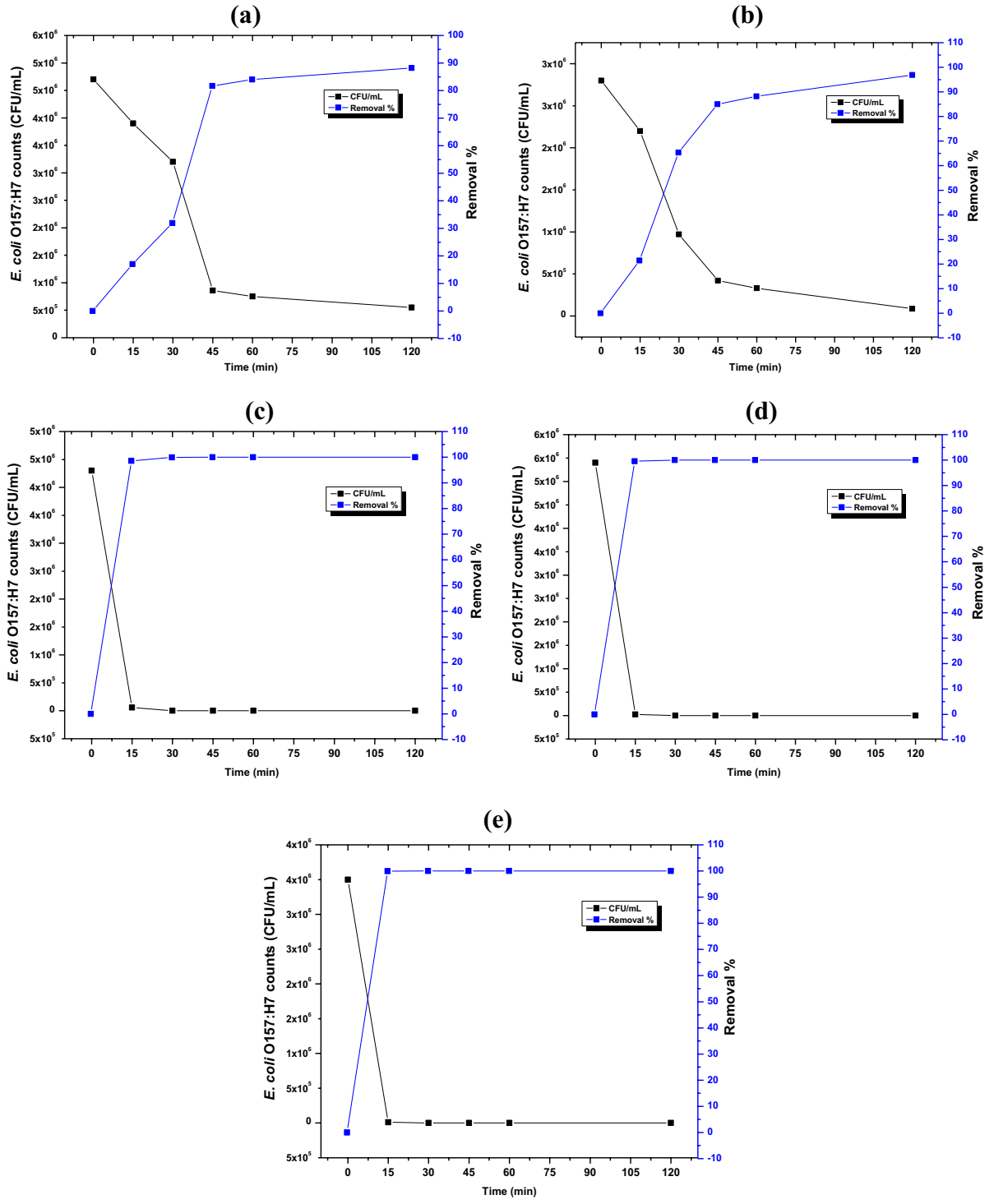

Fig. 10 Pathogenic *E. coli* O157:H7 counts and their removal % using different concentrations of MoS_2 nanoparticle. **a** 50 μg.mL^{-1}, **b** 100 μg.mL^{-1}, **c** 250 μg.mL^{-1}, **d** 500 μg.mL^{-1}, and **e** 1000 μg.mL.$^{-1}$

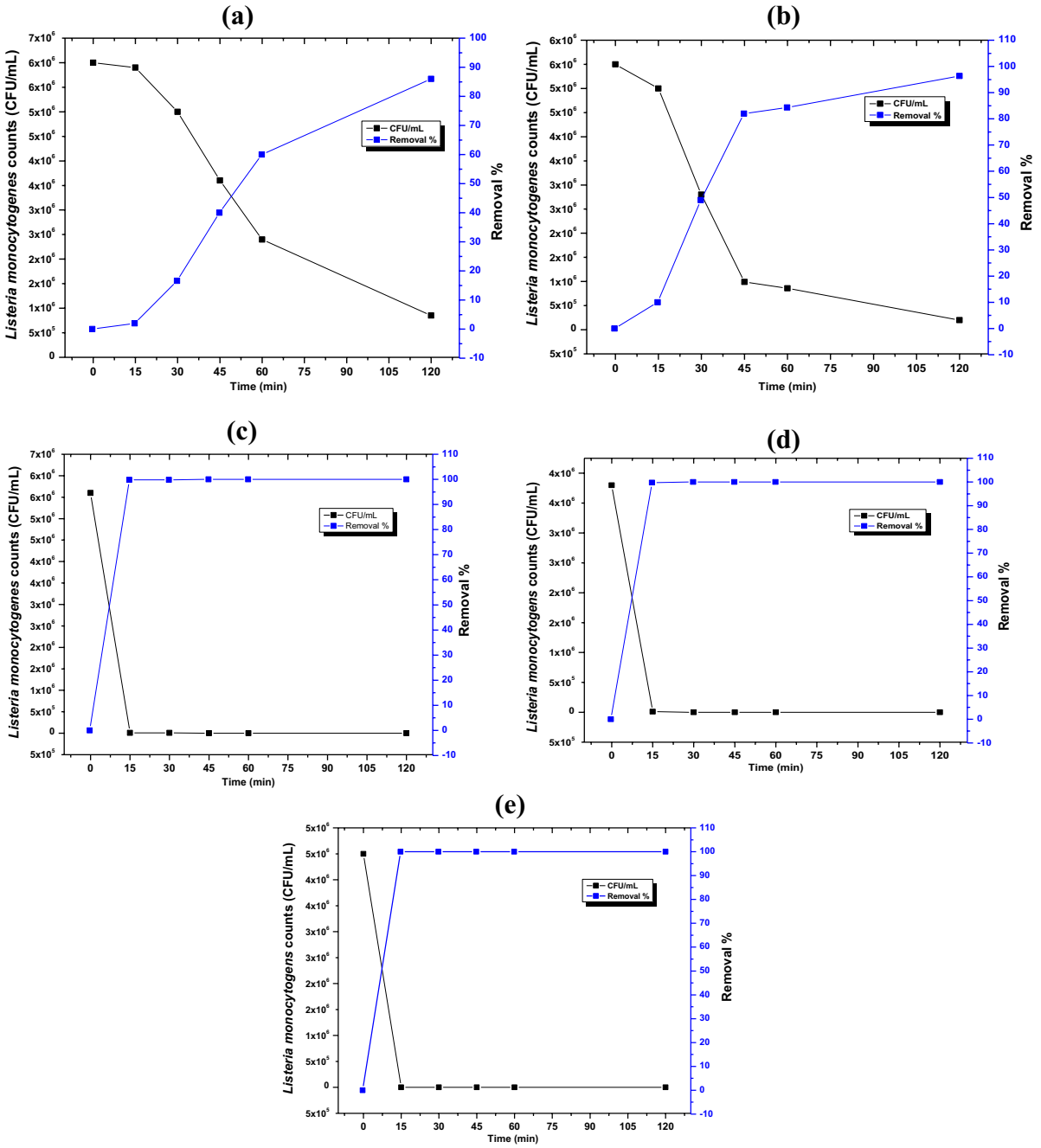

Fig. 11 *Listeria monocytogenes* counts and their removal % using different concentrations of MoS_2 nanoparticle. **a** 50 μg.mL^{-1}, **b** 100 μ μg.mL^{-1}, **c** 250 μg.mL^{-1}, **d** 500 μg.mL^{-1}, and **e** 1000 μg.mL.$^{-1}$

86 and 97% of *Candida albicans* have been removed with 50 and 100 μg.mL^{-1} of MoS_2 after 120 min as a contact time (Fig. 12a, b). Moreover, complete inactivation for *Candida albicans* is exhibited with 1000, 500, and 250 μg.mL^{-1} of MoS_2 after contact times 45, 60, and 60 min (Fig. 12c, d, e). It is observed that 100% removal of *Candida albicans* (45 min) consumed more time than that needed for both *E. coli* O157:H7 and

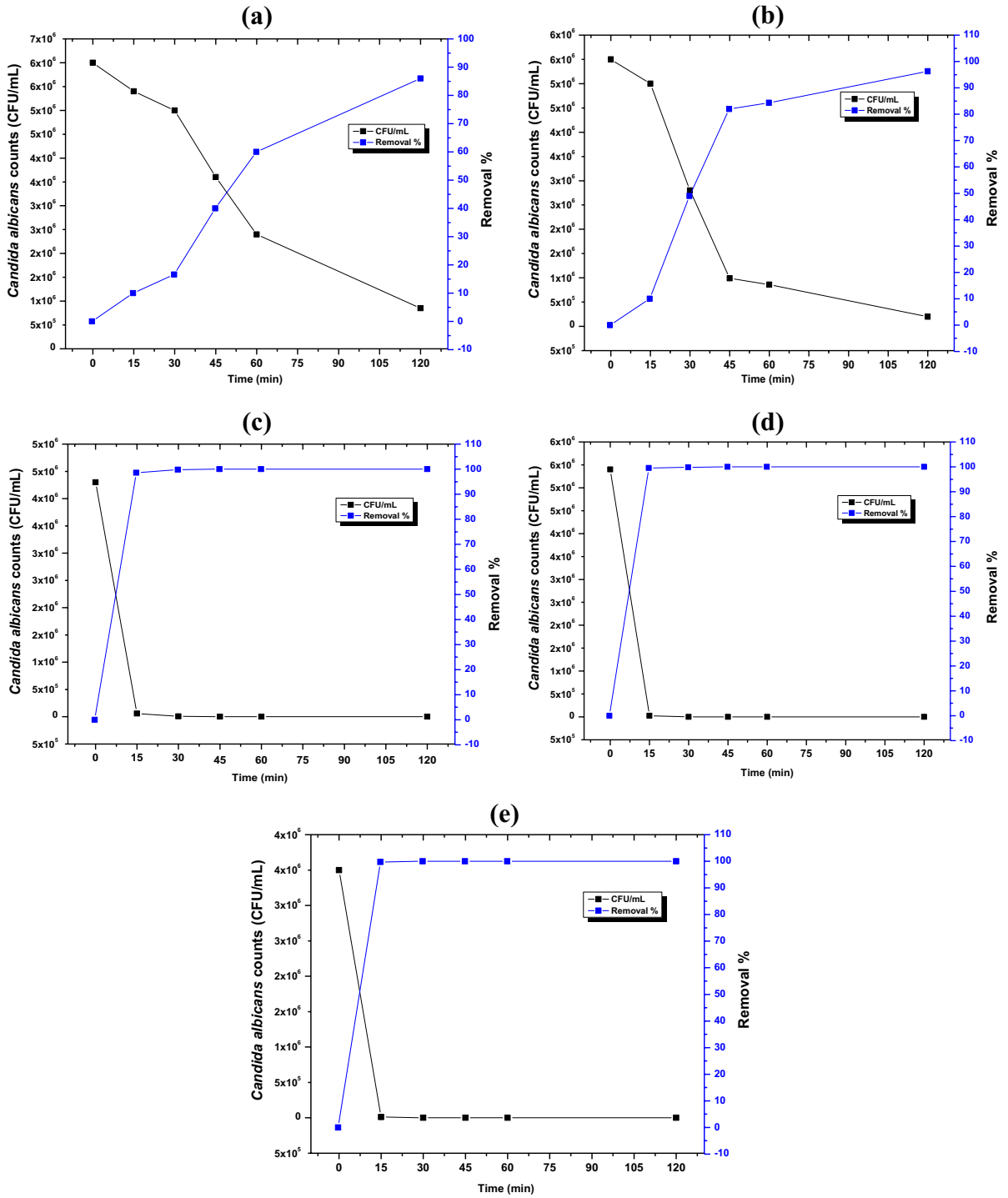

Fig. 12 *Candida albicans* counts and their removal % using different concentrations of MoS_2 nanoparticle. **a** 50 µg.mL^{-1}, **b** 100 µg.mL^{-1}, **c** 250 µg.mL^{-1}, **d** 500 µg.mL^{-1}, and **e** 1000 µg.mL.$^{-1}$

Listeria monocytogenes (30 min). The mode of action of MoS_2 disinfection against microorganisms could be due to the ability of MoS_2 nanosheets to block and cover the microbial cell walls. Moreover, dissolution of MoS_2 nanosheets leads to acidification of aquatic media whereas lowering pH leads to cell walls shrinking and consequently microbial cells destroying [67]. The cell membrane of microbial cells is frequently injured through direct contact between the microorganisms and the very sharp edges of the MoS_2 nanosheets [67, 68].

Conclusion

In brief, a simple cost-effective efficient hydrothermal method has been used for the synthesis of MoS_2 nanosheet photocatalyst. The improvement in sun light-driven photocatalytic Cr (VI) reduction is due to the high adsorption ability for MoS_2 and enhanced charge separation because of the nanosheet structure formation and improved light absorption. The photocatalytic activity of MoS_2 nanosheets has been tested by photoreduction of Cr^{6+} to Cr^{3+} under a solar simulator. There is Cr^{6+} adsorption and photoreduction as well as Cr^{3+} desorption. The pH value of the reaction solution is crucial to the adsorption of Cr^{6+} and photoreduction to Cr^{3+} on the MoS_2 surface. Additionally, the activity of (1 T/2H) MoS_2 nanosheets is investigated for photodegradation of pharmaceutical pollutants (cefadroxil, cefotaxime, meloxicam, ibuprofen, and ciprofloxacin) from wastewater and it is found that (1 T/2H) MoS_2 nanosheets are a non-selective proficient photocatalyst for the decontamination of pharmaceutical pollutants. 50, 100, 250, and 500 µg. mL−1 of MoS2 nanosheets are nontoxic (EC50 ≥100) and ecofriendly to use for water purification 250 µg.mL^{-1} of MoS2 nanosheets can totally inactivate the tested microbial pathogens within 30 min for *E. coli* O157:H7 and *L. monocytogenes* and 45 min for *Candida albicans*. Our current research is expected to give a simple and effective method for photocatalytic decontamination of hexavalent chromium, pharmaceuticals, and microbial pathogen disinfection.

Author contribution Reem. Mohammed: conceptualized the research idea, conducted all the analysis, collected literatures and data, and drafted and revised the manuscript. Mohamed Eid M. Ali, supervised the work, and reviewed the manuscript. Reem. Mohammed: revised manuscript and polished all figures. All authors read and approved the final manuscript.

Funding Open access funding provided by The Science, Technology & Innovation Funding Authority (STDF) in cooperation with The Egyptian Knowledge Bank (EKB).

Data availabilty All the data and materials applied in the study could be available from the corresponding author only on academic or other non-business requests.

Declarations

Ethics approval and consent to publish, participate We confirm that this manuscript had not been published elsewhere before and would not be considered to be published on other journals.

Competing interests The authors declare that they have no conflict of interest.

Open Access This article is licensed under a Creative Commons Attribution 4.0 International License, which permits use, sharing, adaptation, distribution and reproduction in any medium or format, as long as you give appropriate credit to the original author(s) and the source, provide a link to the Creative Commons licence, and indicate if changes were made. The images or other third party material in this article are included in the article's Creative Commons licence, unless indicated otherwise in a credit line to the material. If material is not included in the article's Creative Commons licence and your intended use is not permitted by statutory regulation or exceeds the permitted use, you will need to obtain permission directly from the copyright holder. To view a copy of this licence, visit http://creativecommons.org/licenses/by/4.0/.

References

1. Ali H, Khan E, Ilahi I (2019) Environmental chemistry and ecotoxicology of hazardous heavy metals: environmental persistence, toxicity, and bioaccumulation. J Chem 2019. https://doi.org/10.1155/2019/6730305
2. Costa M (2003) Potential hazards of hexavalent chromate in our drinking water. Toxicol Appl Pharmacol 188(1):1–5. https://doi.org/10.1016/S0041-008X(03)00011-5
3. Peng H, Guo J (2020) Removal of chromium from wastewater by membrane filtration, chemical precipitation, ion exchange, adsorption electrocoagulation, electrochemical reduction, electrodialysis, electrodeionization, photocatalysis and nanotechnology: a review. Environ Chem Lett 18(6):2055–2068. https://doi.org/10.1007/s10311-020-01058-x
4. Barakat M (2011) New trends in removing heavy metals from industrial wastewater. Arab J Chem 4(4):361–377. https://doi.org/10.1016/j.arabjc.2010.07.019
5. Singh A, Pal DB, Mohammad A, Alhazmi A, Haque S, Yoon T, Srivastava N, Gupta VK (2022) Biological remediation technologies for dyes and heavy metals in wastewater treatment: new insight. Bioresour Technol 343:126154. https://doi.org/10.1016/j.biortech.2021.126154

6. Weng C-H, Sharma Y, Chu S-H (2008) Adsorption of Cr (VI) from aqueous solutions by spent activated clay. J Hazard Mater 155(1–2):65–75. https://doi.org/10.1016/j.jhazmat.2007.11.029
7. Bandara P, Peña-Bahamonde J, Rodrigues D (2020) Redox mechanisms of conversion of Cr (VI) to Cr (III) by graphene oxide-polymer composite. Sci Rep 10(1):1–8. https://doi.org/10.1038/s41598-020-65534-8
8. Prashanth L, Kattapagari KK, Chitturi RT, Baddam VRR, Prasad LK (2015) A review on role of essential trace elements in health and disease. J Dr NTR Univ Health Sci 4(2):75. https://doi.org/10.4103/2277-8632.158577
9. Liu W, Li J, Zheng J, Song Y, Shi Z, Lin Z, Chai L (2020) Different pathways for Cr (III) oxidation: implications for Cr (VI) reoccurrence in reduced chromite ore processing residue. J Environ Sci Technol 54(19):11971–11979. https://doi.org/10.1021/acs.est.0c01855
10. Banupriya C, Srinivasan K, Rajasekar A, Murugan K, Benelli G, Dinakaran K (2017) Metal enhanced fluorescence mediated assay for the detection of Hg (II) ions in aqueous solution from rhodamine B and Silver nanoparticle embedded silica thin film. Chin Chem Lett 28:1399–1405
11. Chakrabarti S, Chaudhuri B, Bhattacharjee S, Ray AK, Dutta BK (2009) Photo-reduction of hexavalent chromium in aqueous solution in the presence of zinc oxide as semiconductor catalyst. Chem Eng J 153(1–3):86–93. https://doi.org/10.1016/j.cej.2009.06.021
12. Banerjee P, Chakrabarti S, Maitra S, Dutta BK (2012) Zinc oxide nano-particles–sonochemical synthesis, characterization and application for photo-remediation of heavy metal. Ultrason Sonochem 19(1):85–93. https://doi.org/10.1016/j.ultsonch.2011.05.007
13. Djellabi R, Ghorab FM, Nouacer S, Smara A, Khireddine O (2016) Cr (VI) photocatalytic reduction under sunlight followed by Cr (III) extraction from TiO_2 surface. Mater Lett 176:106–109. https://doi.org/10.1016/j.matlet.2016.04.090
14. Wei X, Wang P, Fu H, Zhao C, Wang C-C (2020) Boosted photocatalytic elimination toward Cr (VI) and organic pollutants over BUC-21/Cd0. 5Zn0. 5S under LED visible Light. Mater Res Bull 129:110903. https://doi.org/10.1016/j.materresbull.2020.110903
15. Mohammed R, Ali MEM, Gomaa E, Mohsen M (2021) Highly stable, reusable, and MW-assisted prepared ZnO nanorods for wastewater decontamination: precursors ratios effect and insights on matrix and pollutants mineralization. J Environ Chem Eng 9(1):104630. https://doi.org/10.1016/j.jece.2020.104630
16. Mohammed R, Ali MEM, Gomaa E, Mohsen M (2020) Green ZnO nanorod material for dye degradation and detoxification of pharmaceutical wastes in water. J Environ Chem Eng 8(5):104295. https://doi.org/10.1016/j.jece.2020.104295
17. Li J, Wei L, Yu C, Fang W, Xie Y, Zhou W, Zhu L (2015) Preparation and characterization of graphene oxide/Ag2CO3 photocatalyst and its visible light photocatalytic activity. Appl Surf Sci 358:168–174. https://doi.org/10.1016/j.apsusc.2015.07.007
18. Mohammed R, Ali MEM, Abdel-Moniem SM, Ibrahim HS (2022) Reusable and highly stable MoS_2 nanosheets for photocatalytic, sonocatalytic and thermocatalytic degradation of organic dyes: comparative study. Nano-Struct Nano-Objects 31:100900. https://doi.org/10.1016/j.nanoso.2022.100900
19. Gupta D, Chauhan V, Kumar R (2020) A comprehensive review on synthesis and applications of molybdenum disulfide (MoS2) material: past and recent developments. Inorg Chem Commun 121:108200. https://doi.org/10.1016/j.inoche.2020.108200
20. Chang K, Hai X, Ye J (2016) Transition metal disulfides as noble-metal-alternative co-catalysts for solar hydrogen production. Adv Energy Mater 6(10):1502555. https://doi.org/10.1002/aenm.201502555
21. Pangajam A, Chandramohan A, Dinakaran K, Harichandran G, Sureshkumar R (2021) Preparation and characterization of graphene nanosheets dispersed pyrrole-chorobenzaldehyde-heptaldehyde conjugated terpolymer nanocomposites for DNA detection. J Solid State Electrochem 25(10):2611–2623. https://doi.org/10.1007/s10008-021-05043-4
22. Gan X, Zhao H, Quan X (2017) Two-dimensional MoS_2: a promising building block for biosensors. Biosens Bioelectron 89:56–71. https://doi.org/10.1016/j.bios.2016.03.042
23. Butler SZ, Hollen SM, Cao L, Cui Y, Gupta JA, Gutiérrez HR, Heinz TF, Hong SS, Huang J, Ismach AF (2013) progress, challenges, and opportunities in two-dimensional materials beyond graphene. ACS Nano 7(4):2898–2926. https://doi.org/10.1021/nn400280c
24. Chen C-A, Lee C-L, Yang P-K, Tsai D-S, Lee C-P (2021) Active site engineering on two-dimensional-layered transition metal dichalcogenides for electrochemical energy applications: a mini-review. Catalyst 11(2):151. https://doi.org/10.3390/catal11020151
25. Srinivasan K, Subramanian K, Murugan K, Benelli G, Dinakaran K (2018) Fluorescence quenching of MoS2 nanosheets/DNA/silicon dot nanoassembly: effective and rapid detection of Hg2+ ions in aqueous solution. Environ Sci Pollut Res 25(11):10567–10576. https://doi.org/10.1007/s11356-018-1472-x
26. Ejigu A, Kinloch IA, Prestat E, Dryfe RA (2017) A simple electrochemical route to metallic phase trilayer MoS_2: evaluation as electrocatalysts and supercapacitors. J Mater Chem 5(22):11316–11330. https://doi.org/10.1039/C7TA02577G
27. Huang H, Cui Y, Li Q, Dun C, Zhou W, Huang W, Chen L, Hewitt CA, Carroll DL (2016) Metallic 1T phase MoS_2 nanosheets for high-performance thermoelectric energy harvesting. Nano Energy 26:172–179. https://doi.org/10.1016/j.nanoen.2016.05.022
28. Duong DL, Yun SJ, Lee YH (2017) van der Waals layered materials: opportunities and challenges. ACS Nano 11(12):11803–11830. https://doi.org/10.1021/acsnano.7b07436
29. Liu T, Liu Z (2018) 2D MoS_2 nanostructures for biomedical applications. Adv Healthc Mater 7(8):1701158. https://doi.org/10.1002/adhm.201701158
30. Miao H, Hu X, Sun Q, Hao Y, Wu H, Zhang D, Bai J, Liu E, Fan J, Hou X (2016) Hydrothermal synthesis of MoS_2 nanosheets films: microstructure and formation mechanism research. Mater Lett 166:121–124. https://doi.org/10.1016/j.matlet.2015.12.010
31. Li Y, Bian Y, Qin H, Zhang Y, Bian Z (2017) Photocatalytic reduction behavior of hexavalent chromium on

hydroxyl modified titanium dioxide. Appl Catal 206:293–299. https://doi.org/10.1016/j.apcatb.2017.01.044
32. Yao Y, Ao K, Lv P, Wei Q (2019) MoS2 coexisting in 1T and 2H phases synthesized by common hydrothermal method for hydrogen evolution reaction. J Nanomater 9(6):844. https://doi.org/10.3390/nano9060844
33. Li Q-H, Dong M, Li R, Cui Y-Q, Xie G-X, Wang X-X, Long Y-Z (2021) Enhancement of Cr (VI) removal efficiency via adsorption/photocatalysis synergy using electrospun chitosan/g-C3N4/TiO2 nanofibers. Carbohydr Polym 253:117200. https://doi.org/10.1016/j.carbpol.2020.117200
34. El-Liethy MA, Elwakeel KZ, Ahmed MS (2018) Comparison study of Ag (I) and Au (III) loaded on magnetic thiourea-formaldehyde as disinfectants for water pathogenic microorganism's deactivation. J Environ Chem Eng 6(4):4380–4390. https://doi.org/10.1016/j.jece.2018.06.028
35. Elwakeel KZ, El-Liethy MA, Ahmed MS, Ezzat SM, Kamel MM (2018) Facile synthesis of magnetic disinfectant immobilized with silver ions for water pathogenic microorganism's deactivation. Environ Sci Pollut Res 25(23):22797–22809. https://doi.org/10.1007/s11356-018-2071-6
36. Sharma C, Badatya S, Srivastava AK, Gupta MK (2021) Unraveling Anomalous Dielectric Phase Transition in Few-Layered 2H/1T MoS_2 Nanosheets. Phys Chem C 125(25):14089–14097. https://doi.org/10.1021/acs.jpcc.1c03430
37. Zhao B, Shen D, Zhang Z, Lu P, Hossain M, Li J, Li B, Duan X (2021) 2D metallic transition-metal dichalcogenides: structures, synthesis, properties, and applications. Adv Funct Mater 31(48):2105132. https://doi.org/10.1002/adfm.202105132
38. Wang C, Wang H, Lin Z, Li W, Lin B, Qiu W, Quan Y, Liu Z, Chen S (2019) In situ synthesis of edge-enriched MoS_2 hierarchical nanorods with 1T/2H hybrid phases for highly efficient electrocatalytic hydrogen evolution. Cryst Eng Comm 21(12):1984–1991. https://doi.org/10.1039/C9CE00159J
39. Doan TLL, Nguyen DC, Prabhakaran S, Kim DH, Tran DT, Kim NH, Lee JH (2021) Single-atom co-decorated MoS2 nanosheets assembled on metal nitride nanorod arrays as an efficient bifunctional electrocatalyst for pH-universal water splitting. Adv Funct Mater 31(26):2100233. https://doi.org/10.1039/C9CE00159J
40. Mustapha S, Tijani J, Ndamitso M, Abdulkareem A, Shuaib D, Amigun A, Abubakar H (2021) Facile synthesis and characterization of TiO2 nanoparticles: X-ray peak profile analysis using Williamson-Hall and Debye-Scherrer methods. Int Nano Lett 11(3):241–261. https://doi.org/10.1007/s40089-021-00338-w
41. Yuan J, Wang F, Patel S, Hu Z-L, Tang M, Lou J (2021) Minimizing the water effect in synthesis of high-quality monolayer MoS2 nanosheets: implications for electronic and optoelectronic devices. ACS Appl Nano Mater 4(8):8094–8100. https://doi.org/10.1021/acsanm.1c01361
42. Leonard N, Ju W, Sinev I, Steinberg J, Luo F, Varela AS, Cuenya BR, Strasser P (2018) The chemical identity, state and structure of catalytically active centers during the electrochemical CO_2 reduction on porous Fe–nitrogen–carbon (Fe–N–C) materials. Chem Sci 9(22):5064–5073. https://doi.org/10.1039/C8SC00491A
43. Majee BP, Srivastava V, Mishra AK (2020) Surface-enhanced Raman scattering detection based on an interconnected network of vertically oriented semiconducting few-layer MoS_2 nanosheets. ACS Appl Nano Mater 3(5):4851–4858. https://doi.org/10.1039/C8SC00491A
44. Gan X, Zhao H, Lei D, Wang P (2020) Improving electrocatalytic activity of 2H-MoS2 nanosheets obtained by liquid phase exfoliation: covalent surface modification versus interlayer interaction. J Catal 391:424–434. https://doi.org/10.1016/j.jcat.2020.09.009
45. Wang S, Zhang D, Li B, Zhang C, Du Z, Yin H, Bi X, Yang S (2018) Ultrastable in-plane 1T–2H MoS_2 heterostructures for enhanced hydrogen evolution reaction. Adv Energy Mater 8(25):1801345. https://doi.org/10.1002/aenm.201801345
46. Zhao W, Liu X, Yang X, Liu C, Qian X, Sun T, Chang W, Zhang J, Chen Z (2020) Synthesis of novel 1t/2h-MoS_2 from moo_3 nanowires with enhanced photocatalytic performance. J Nanomater 10(6):1124. https://doi.org/10.3390/nano10061124
47. Liu M, Li X, Xu Z, Li B, Chen L, Shan N (2012) Synthesis of chain-like MoS_2 nanoparticles in W/O reverse microemulsion and application in photocatalysis. Sci Bull 57(30):3862–3866. https://doi.org/10.1007/s11434-012-5339-0
48. Cheng J, Han L, Wei Y, Chen Q. Enhancement of photocatalytic property on ZnS/MoS_2 composite under visible light irradiation. MATEC Web Conf. 2017: EDP Sciences; 2017: 01008. https://doi.org/10.1051/matecconf/201710801008
49. Lv X, Guo W, Song J, Fu Y (2022) Dynamic 1T-2H mixed-phase MoS_2 enables high-performance Li-organosulfide battery. Small 2105071. https://doi.org/10.1002/smll.202105071
50. Hu X-J, Wang J-S, Liu Y-G, Li X, Zeng G-M, Bao Z-L, Zeng X-X, Chen A-W, Long F (2011) Adsorption of chromium (VI) by ethylenediamine-modified cross-linked magnetic chitosan resin: isotherms, kinetics and thermodynamics. J Hazard Mater J Hazard Mater 185(1):306–314. https://doi.org/10.1016/j.jhazmat.2010.09.034
51. Sun H, Wu T, Zhang Y, Ng DH, Wang G (2018) Structure-enhanced removal of Cr (vi) in aqueous solutions using MoS_2 ultrathin nanosheets. New J Chem 42(11):9006–9015. https://doi.org/10.1039/C8NJ01062E
52. Di Z-C, Li Y-H, Luan Z-K, Liang J (2004) Adsorption of chromium (VI) ions from water by carbon nanotubes. Adsorp Sci Technol 22(6):467–474. https://doi.org/10.1260/0263617042879537
53. Wu Z, Li S, Wan J, Wang Y. Cr (VI) adsorption on an improved synthesised cross-linked chitosan resin. J Mol Liq 170:25–29 https://doi.org/10.1016/j.molliq.2012.03.016
54. Zhang T, Wang W, Zhao Y, Bai H, Wen T, Kang S, Song G, Song S, Komarneni S (2021) Removal of heavy metals and dyes by clay-based adsorbents: from natural clays to 1D and 2D nano-composites. Chem Eng J 420:127574. https://doi.org/10.1016/j.cej.2020.127574
55. Maneechakr P, Karnjanakom S (2021) Facile utilization of magnetic MnO_2@ Fe_3O_4@ sulfonated carbon sphere for selective removal of hazardous Pb (II) ion with an excellent capacity: adsorption behavior/isotherm/kinetic/thermodynamic studies. J Environ Chem Eng 9(5):106191. https://doi.org/10.1016/j.jece.2021.106191

56. Kar S, Equeenuddin S (2019) Adsorption of hexavalent chromium using natural goethite: isotherm, thermodynamic and kinetic study. J Geol Soc India 93(3):285–292. https://doi.org/10.1007/s12594-019-1175-z
57. Wu Q, Zhao J, Qin G, Wang C, Tong X, Xue S (2013) Photocatalytic reduction of Cr (VI) with TiO2 film under visible light. Appl Catal 142:142–148. https://doi.org/10.1016/j.apcatb.2013.04.056
58. Chand R, Ramalingam S, Neethirajan S (2018) A 2D transition-metal dichalcogenide MoS $_2$ based novel nanocomposite and nanocarrier for multiplex miRNA detection. 10(17):8217–8225. https://doi.org/10.1039/C8NR00697K
59. Ali GA, Thalji MR, Soh WC, Algarni H, Chong KF. One-step electrochemical synthesis of MoS_2/graphene composite for supercapacitor application. J Solid State Electrochem 24(1):25–34. https://doi.org/10.1007/s10008-019-04449-5
60. Zeng X, Niu L, Song L, Wang X, Shi X, Yan J (2015) Effect of polymer addition on the structure and hydrogen evolution reaction property of nanoflower-like molybdenum disulfide. Metals 5(4):1829–1844. https://doi.org/10.3390/met5041829
61. Li Y, Wang X, Liu M, Luo H, Deng L, Huang L, Wei S, Zhou C, Xu Y (2019) Molybdenum disulfide quantum dots prepared by bipolar-electrode electrochemical scissoring. J Nanomater 9(6):906. https://doi.org/10.3390/nano9060906
62. Ibrahim S, El-Liethy MA, Abia ALK, Abdel-Gabbar M, Al Zanaty AM, Kamel MM (2020) Design of a bioaugmented multistage biofilter for accelerated municipal wastewater treatment and deactivation of pathogenic microorganisms. Sci Total Environ 703:134786. https://doi.org/10.1016/j.scitotenv.2019.134786
63. Zou W, Li X, Li C, Sun Y, Zhang X, Jin C, Jiang K, Zhou Q, Hu X (2020) Influence of size and phase on the biodegradation, excretion, and phytotoxicity persistence of single-layer molybdenum disulfide. ES&T 54(19):12295–12306. https://doi.org/10.1021/acs.est.0c02642
64. Li K, Wang Z, Zeng H, Sun J, Wang Y, Zhou Q, Hu X (2021) Surface atomic arrangement of nanomaterials affects nanotoxicity. Nanotoxicology 15(1):114–130. https://doi.org/10.1080/17435390.2020.1844915
65. Teo WZ, Chng ELK, Sofer Z, Pumera M (2014) Cytotoxicity of exfoliated transition-metal dichalcogenides (MoS_2, WS_2, and WSe_2) is lower than that of graphene and its analogues. Chem Eur J 20(31):9627–9632. https://doi.org/10.1002/chem.201402680
66. Ahmad N, Abdullah N, Yasin F (2020) Toxicity assessment of reduced graphene oxide and titanium dioxide nanomaterials on gram-positive and gram-negative bacteria under normal laboratory lighting condition. Toxicol Rep 7:693–699. https://doi.org/10.1016/j.toxrep.2020.04.015
67. Zhang X, Zhang W, Liu L, Yang M, Huang L, Chen K, Wang R, Yang B, Zhang D, Wang J (2017) Antibiotic-loaded MoS_2 nanosheets to combat bacterial resistance via biofilm inhibition. Nanotechnology 28(22):225101. https://doi.org/10.1088/1361-6528/aa6c9b
68. Bae M, Oh JK, Liu S, Nagabandi N, Yegin Y, DeFlorio W, Cisneros-Zevallos L, Scholar E (2021) Nanotoxicity of 2D molybdenum disulfide, MoS_2, nanosheets on beneficial soil bacteria, Bacillus cereus and Pseudomonas aeruginosa. Nanomater 11(6):1453. https://doi.org/10.3390/nano11061453

Publisher's note Springer Nature remains neutral with regard to jurisdictional claims in published maps and institutional affiliations.